Theoretical and Applied Fracture Mechanics 145 (2026) 105586

Contents lists available at ScienceDirect

Theoretical and Applied Fracture Mechanics

journal homepage: www.elsevier.com/locate/tafmec

Failure mechanisms along patterned bimaterial interfaces

Charline van Innis [a,b], Julie Teuwen [a], Sofia Teixeira de Freitas [a,c,*]

[a] Faculty of Aerospace Engineering, Delft University of Technology, Delft, Netherlands
[b] BATir, Building, Architecture and Town Planning Department, Université Libre de Bruxelles, Brussels, Belgium
[c] IDMEC, Instituto Superior Tecnico, Universidade de Lisboa, Lisbon, Portugal

ARTICLE INFO

Keywords:
Deflection
Penetration
Toughness
Cohesive law
Interface

ABSTRACT

Further development of thermoplastic composites for advanced structural applications, such as in aerospace, requires tough interfaces at bimaterials junctions such as composite-metal interfaces. Mode I failure being the most critical failure mode of interfaces, surface roughening or patterning techniques are commonly used to improve the mode I interface toughness. Patterning typically involves creating grooves on the surface via laser ablation or 3D printing. However, crack propagation may follow two distinct paths: along the groove pattern (interfacial failure) or through the polymer within the grooves (cohesive failure). Cohesive failure is often the toughest mechanism. However, design criteria linking groove geometry to joint materials are currently lacking. This study investigates the influence of groove dimensions, joint dimensions, and material and interface properties on the resulting failure mechanism using a cohesive zone model. First, a small-scale yielding (SSY) model is developed. The results indicate that the characteristic fracture length of the material filling the grooves plays a critical role in determining the failure mechanism. Specifically, cohesive failure is promoted when the groove depth is at least ten times greater than the characteristic length, and when the groove aspect ratio (depth-to-width) exceeds 10. Additionally, filling the grooves with a more compliant material, such as a polymer, helps to prevent interfacial failure. Finally, a double-cantilever model is developed, indicating that the loading configuration significantly influences the failure mechanisms taking place. For the DCB configuration, crack propagation along the interface is promoted, compared to the SSY case, owing to the bending of the adherends.

1. Introduction

Over the last decade, thermoplastic composites (TPC) made of high-performance polymers such as polyetherimide (PEI), polyether ether ketone (PEEK), polyetherketoneketone (PEKK) or low-melt polyarylatherketone (LMPAEK) have been intensively deployed in advanced structures such as aircrafts [1]. Like thermoset composites, they offer high strength and stiffness to weight ratio. However, TPCs are tougher and exhibit a higher impact resistance compared to their traditionally used thermoset counterpart [1]. Further deployment of TPCs requires the assembly of these materials with other materials such as metals to design complex structures, as well as to design fiber-metal laminates. Often, mechanical fasteners are used to join dissimilar materials in advanced applications [2,3]. However, this results in additional weight and thus additional fuel consumption. For both thermoset and thermoplastic composites, adhesive bonding is an alternative, but adhesive joints suffer from low toughness [2]. However, unlike thermoset composites, TPCs can be welded through ultrasonic, resistance or induction welding [4,5]. In addition, bonding can also be performed during composite manufacturing through co-consolidation [6]. The critical point regarding the failure of the assembly is the interface between the TPC and the other material as it is prone to failure. The reliability of such assemblies can be improved through surface treatments and new design strategies resulting in enhanced interface fracture toughness.

To improve the durability of TPC-metal assemblies, interface toughening strategies have been investigated. Mechanical interlocking is known to improve adhesion and interface toughness. Mechanical interlocking is related to surface roughness that can be created through sandblasting, polishing or laser ablation [6–8]. Interface patterning also results in enhanced mechanical interlocking. As shown in Fig. 1, interface patterning refers to the design of grooves [9–15], pits [13,14,16], pins [17] or any other pattern [16,18] with predefined dimensions. Grooves can exhibit various geometries, such as rectangular, triangular, or elliptical cross-sections and can be arranged in different configurations: parallel or perpendicular to the crack propagation direction, or distributed in a grid pattern [13,19–21]. Such patterns are achieved through laser patterning via laser ablation [11,15,22,23], additive

* Corresponding author at: Faculty of Aerospace Engineering, Delft University of Technology, Delft, Netherlands.
E-mail address: S.TeixeiraDeFreitas@tudelft.nl (S. Teixeira de Freitas).

https://doi.org/10.1016/j.tafmec.2026.105586
Received 26 January 2026; Received in revised form 13 March 2026; Accepted 24 March 2026
Available online 27 March 2026

Nomenclature

Abbreviations

DCB	Double Cantilever Beam
FE	Finite element
LMPAEK	Low-melt polyarylatherketone
PEEK	Polyether ether ketone
PEI	Polyetherimide
PEKK	Polyetherketoneketone
SSY	Small scale yielding
TPC	Thermoplastic composite
TSL	Traction-separation law

Symbols

A	Groove aspect ratio [−]
α	First Dundur's parameter [−]
B	Width of partly built-in beam [mm]
β	Second Dundur's parameter [−]
D	Groove depth [mm]
d	Horizontal distance from crack tip at which $\psi = \overline{\psi}$ [mm]
δ_c	Critical opening displacement [mm]
δ_c^i	Critical opening displacement of the interface [mm]
δ^N	Normal opening displacement [mm]
δ^T	Tangential opening displacement [mm]
E	Young's modulus of partly built-in beam [MPa]
E_i	Young's modulus of material I [MPa]
El_1	First auxiliary element
El_2	Second auxiliary element
ε	Oscillation parameter [−]
ε_{xx}	Longitudinal strain in DCB beam [−]
f_{y-Nbot}	Force applied on node N_{bot} [N]
f_{yNC}	Force applied on the control node [N]
f_{y-Ntop}	Force applied on node N_{top} [N]
G	Energy release rate [J/m^2]
Γ_c	Cohesive energy [J/m^2]
Γ_c^i	Cohesive energy of the interface [J/m^2]
Γ_c^1	Cohesive energy of material 1 [J/m^2]
Γ_{Ic}	Mode I cohesive energy [J/m^2]
Γ_{IIc}	Mode II cohesive energy [J/m^2]
h	Thickness of partly built-in beam [mm]
h_e	Length over which the partly built-in beam is built-in [mm]
h_i	Thickness of material I [mm]
i	subscript referring to material I ($i = 1,2$)
K	Stress intensity factor [MPa*m$^{0.5}$]
K_{coh}	Stiffness of the elastic part of the cohesive law [MPa/mm]
K_I^∞	Remote mode I stress intensity factor [MPa*m$^{0.5}$]
K_{II}	Crack tip mode II stress intensity factor [MPa*m$^{0.5}$]
K_{II}^∞	Remote mode II stress intensity factor [MPa*m$^{0.5}$]
L	Groove length [mm]
l	Length of partly built-in beam [mm]
l_{cz}	Fracture process zone length [mm]
l_s^i	Characteristic length of the interface [mm]
l_s^1	Characteristic length of material 1 [mm]
N_{bot}	Node of second auxiliary element located on lower beam
N_c	Control node
N_{top}	Node of second auxiliary element located on upper beam
N_1	Node of first auxiliary element
N_2	Node of first auxiliary element
μ_i	Shear coefficient of material I [MPa]
ν_i	Poisson ratio of material i [−]
ψ	Phase angle at a distance d from crack tip [rad]
$\overline{\psi}$	Phase angle at a distance x from crack tip, depends on ψ [rad]
R	Radius of SSY model [mm]
S	Spacing between grooves [mm]
σ_c	Cohesive strength [MPa]
σ_c^i	Cohesive strength of the interface [MPa]
σ_c^1	Cohesive strength of material 1 [MPa]
σ_{yy}	Tensile stress [MPa]
τ_c	Shear cohesive strength [MPa]
τ_{yx}	Shear stress in y-x plane [MPa]
θ	Angle between the crack plane and a node from out circle in SSY model [rad]
u_{Ncy}	Vertical displacement of Node N_c [mm]
u_{N1y}	Vertical displacement of Node N_1 [mm]
u_{N2y}	Vertical displacement of Node N_2 [mm]
u_x	Horizontal displacement [mm]
u_y	Vertical displacement [mm]
u_{y-BC}	Vertical displacement applied to partly built-in beam [mm]
x	Horizontal distance from crack tip [mm]

manufacturing [19,24,25], lithography [10,26,27] or conventional machining [20,21]. The dimensions of the patterns such as the depth, the width or the spacing between the features play an important role as they influence the failure mechanism taking place along the interface [9,10,13,22,27]. Indeed, depending on the dimensions, either adhesive failure along the interface or cohesive failure in the thermoplastic material filling the grooves takes place [10,28], as illustrated in Fig. 1. A combination of both is also possible and is referred to as mixed-mode failure.

Some researchers also investigated dual-scale patterning with a smaller pattern created on a pattern characterized by a larger-scale such as those observed on frog-pads [29]. The deployment of additive manufacturing allowed the development of more complex patterns such as body and face centered lattices [24]. Additive manufacturing also inherently introduces surface roughness on the metal substrate, thereby enhancing mechanical interlocking [30,31].

No matter the type of pattern created, the geometry and dimensions of the features significantly influence the failure mechanisms taking place along the interface. In addition to influence the failure of the interface, they also influence the wetting of the metal substrate by the TP material [32] in the case of TPC-metal joints. For example, with deep and narrow grooves or pits, air tends to be trapped in the interface holes [11,16]. Currently, the literature does not provide a clear consensus on how pattern dimensions influence the failure mode, whether the interface fails adhesively (Fig. 1e), cohesively (Fig. 1d), or through a combination of both, often described as mixed mode failure. In this study, we aim to explore the factors that govern the crack path along a patterned interface using finite element modelling.

In the current study, rectangular grooves, running perpendicular to the crack propagation direction are used as pattern. When the crack reaches the groove, it can either follow the groove pattern leading to interfacial failure or propagate into the material filling the groove. The two competitive fracture mechanisms are crack deflection and crack penetration. Crack penetration refers to cohesive failure of the material filling the groove, i.e. the thermoplastic resin, as shown in Fig. 1d, while crack deflection refers to interfacial failure with a crack propagating along the patterned interface, as illustrated in Fig. 1e. Cohesive failure is often believed to be the toughest mechanism, and is thus the one to be favored [6,18].

Competition between crack deflection and penetration at an

interface has been investigated by Parmigiani and Thouless [33], He and Hutchinson [34] and Leguillon and co-workers [35,36]. Among them, only Parmigiani and Thouless [33] use cohesive elements. They consider a crack propagating perpendicular to an interface between two materials A and B, with a crack initially located in material A. They reported greater influence of the cohesive strength on the crack path than of the cohesive energy (fracture toughness). Crack deflection along the interface is reported to take place if the cohesive strength of material B is at least three times higher than that of the interface, in the absence of elastic mismatch between materials A and B, i.e. A and B are characterized by the same Young's modulus [33]. The critical cohesive strength value above which crack deflection takes place is influenced by the elastic mismatch between the two materials forming the interface. A more compliant, i.e. lower Young's modulus, material ahead of the interface, i.e. material B, promotes crack penetration, increasing the critical cohesive strength ratio. In addition, the ratio between the fracture length scale and the specimen dimensions also influences the failure mechanism taking place at the interface. Increasing the fracture length scale prevents crack deflection. Experimentally, the mode I toughness of joints is determined through double cantilever beam (DCB) tests [37]. It has been reported that depending on the beam thickness, and thus on the beam bending stiffness, and on adhesive properties, crack deflection and subsequent propagation in the composite adherend can be influenced [38]. Thinner adherends promote crack deflection in composite substrates due to the larger strains developing in the adherends.

The aim of the present work is to understand the fracture behaviour and to determine design guidelines for patterned interfaces depending on the cohesive strength and toughness of the interface and the material filling the grooves. A parametric finite element (FE) study is conducted to determine under which conditions the crack propagates along the patterned interface or cohesively in the material filling the grooves, i.e. in the thermoplastic resin in the case of TPC-metal joints. To investigate the influence of the cohesive zone properties, the material properties and groove dimensions on the failure mechanism, a small-scale yielding (SSY) finite element model is developed (Fig. 2a). This model allows to eliminate the effects from the testing geometry, so that pure mode I is applied at the crack tip. In the second stage, a FE DCB model is developed in order to consider the influence of the DCB geometry on the failure mechanism (Fig. 2b). In the DCB configuration, the two adherends are considered to be made of the same material to remove effects originating from dissimilar adherends such as the introduction of a slight mode II at the crack tip [39]. The two models are detailed in Section 2.

2. Finite element modelling

Two finite element models, shown in Fig. 2, are developed in the present study. The first one is a small-scale yielding model (Fig. 2a) as done by Hutchinson and Tvergaard [40–42], with details provided in section 2.1. The second model is a double cantilever beam model (Fig. 2b). In both models, the interface is patterned with rectangular grooves with sharp edges, as detailed in Sections 2.1 and 2.2. Sharp edges are considered to avoid considering the influence of the radius associated to corner rounding. Both models involve cohesive elements to model the interface, detailed in Section 2.3. The first model allows investigating the influence of the material properties, the cohesive zone properties and the groove dimensions with respect to a characteristic length scale (Section 2.3). The use of this model is motivated by the fact that in assemblies such as adhesive joints, the mechanical response depends on the adhesive and adherend thickness [43], but also on the loading configuration. Consequently, results obtained with one type of joint, for example DCB, lap-shear joint or tensile butt joint cannot be generalized due to various loading modes and structural size effects. SSY model enables elimination of the influence of the joint geometry on the failure mechanisms which is thus only dependent upon the loading. In order to investigate the influence of the joint geometry on the failure mechanism taking place along the interface, a DCB model is developed. Consequently, the same parameters are investigated with the DCB model as with the SSY model. However, as the bending stiffness [38] is expected to also play a role in the failure mechanism taking place, the material 2 thickness h_2, commonly referred to as the adherend thickness

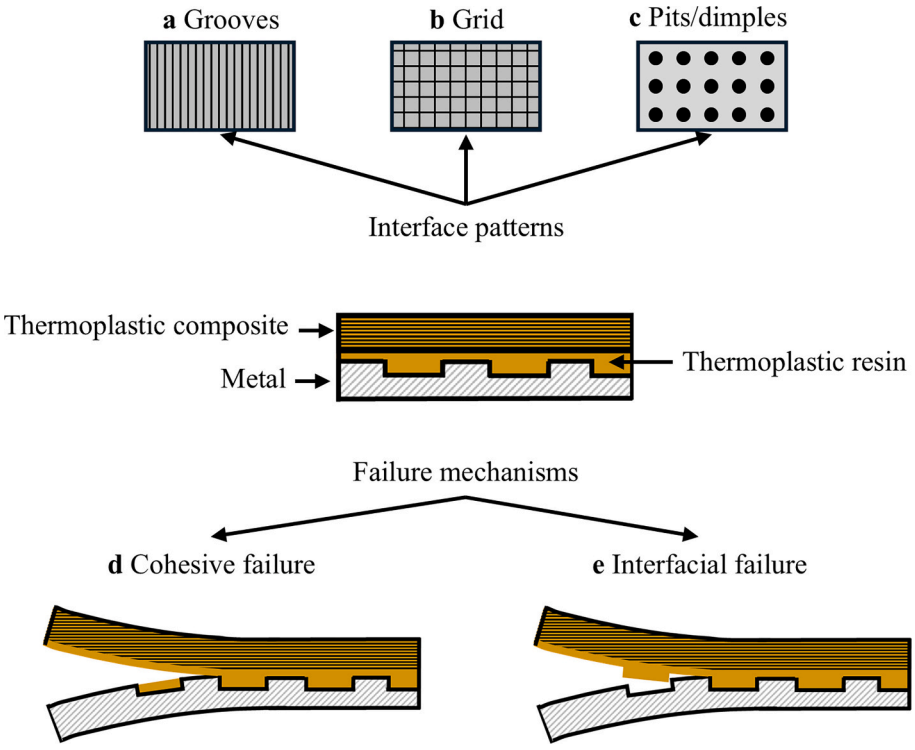

Fig. 1. Toughening of thermoplastic composite-metal interface through patterning: a) grooves, b) grid, c) pits/dimples, and the possible failure mechanisms: d) cohesive failure corresponding to crack penetration in the filling material and e) interfacial failure corresponding to deflection along the interface.

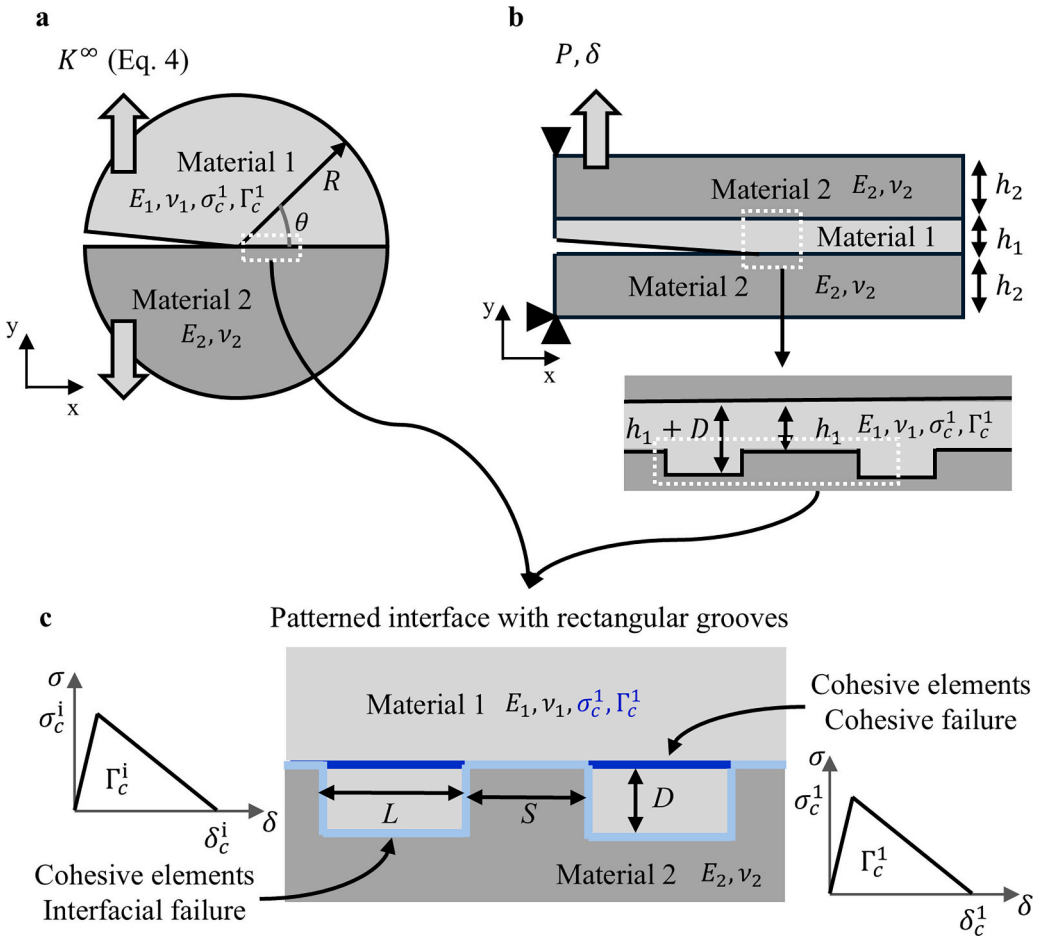

Fig. 2. Finite element geometries: a) small-scale yielding model and b) double cantilever beam model considering similar adherends made of Material 2 of thickness h_2 and Material 1 interlayer of thickness h_1. c) Schematic representation of the grooves at the interface characterized by a depth D, a length L and a spacing S and representation of the two cohesive zones used in the model corresponding to the two possible crack paths, i.e. cohesive in material 1 (dark blue) or along the interface (light blue). (For interpretation of the references to colour in this figure legend, the reader is referred to the web version of this article.)

in the adhesive joints community, has to be considered as additional parameter. Simulations are run using the Abaqus FE software. The mesh is generated using the open-access mesh generator Gmsh through Python scripts.

2.1. Small-scale yielding model (SSY)

The model geometry is shown in Fig. 2a. It is made of semi-circular parts of radius R. The upper part is made of Material 1 while the lower part is made of Material 2. These two materials are perfectly elastic materials characterized by a Young's modulus E_i and a Poisson ratio ν_i with the subscript i identifying the material. The elastic mismatch between these two materials is quantified by the first and second Dundur's parameters [44], denoted by α and β, (respectively)

$$\alpha = \frac{(1-\nu_1)/\mu_1 - (1-\nu_2)/\mu_2}{(1-\nu_1)/\mu_1 + (1-\nu_2)/\mu_2} \tag{1}$$

$$\beta = 0.5\,\frac{(1-2\nu_1)/\mu_1 - (1-2\nu_2)/\mu_2}{(1-\nu_1)/\mu_1 + (1-\nu_2)/\mu_2} \tag{2}$$

μ_i is the shear modulus of material $i = 1,2$ in Eqs. 1 and 2 and is given by $\mu_i = E_i/2(1+\nu_i)$.

At the center of the model, grooves, shown in Fig. 2c, are inserted in the bottom part. These grooves are filled with Material 1. The grooves are characterized by a depth D, a length L and are spaced by a distance S. The radius R has to be significantly larger than the pattern dimensions [40,42,45,46] and is therefore fixed to $R = 1000(L+S)$. To model the two potential failure mechanisms, two cohesive zones are introduced (see section 2.3 for the cohesive zone models). One is placed along the interface between the two materials (light blue in Fig. 2c) while the second one is introduced in Material 1 (dark blue in Fig. 2c). A K-field is applied as boundary displacement (Eq. 4) which depends on the remote stress intensity factor K given by Eq. 3 [41].

$$|K| = \sqrt{\frac{2G}{(1-\beta^2)}\left(\frac{1-\nu_1^2}{E_1} + \frac{1-\nu_2^2}{E_2}\right)^{-1}} \tag{3}$$

G is the interface energy release rate. The displacement field has two components: the horizontal component u_x and the vertical component u_y. If it is assumed that $\nu_1 = \nu_2 = \nu$, the displacement field [41] is given by

$$u_x + iu_y = \frac{|K|}{\mu_1 2\cosh(\pi\varepsilon)}\sqrt{\frac{R}{2\pi}}\left[\frac{(3-4\nu)e^{i\theta/2+\varepsilon(\theta-\pi)-i\overline{\psi}}}{1-2\varepsilon i} - \frac{e^{-i\theta/2-\varepsilon(\theta-\pi)-i\overline{\psi}}}{1-2\varepsilon i} - i\sin\theta e^{i\theta/2+\varepsilon(\theta-\pi)+i\overline{\psi}}\right], \tag{4}$$

where θ is the angle between the crack plane and the corresponding node on the outer circle as shown in Fig. 2a. $\overline{\psi}$, given by Eq. 5, is the phase angle measuring the relative amount of shear to normal stress at a distance x from the crack tip along the crack plane and depends on the remote mode-mixity, K_{II}^∞/K_I^∞, with K_I^∞ and K_{II}^∞ being the mode I and

mode II remote stress intensity factors. d is the distance from the crack tip at which the phase angle is known and is equal to ψ.

$$\overline{\psi}(x) = \psi(d) + \varepsilon \ln\left(\frac{x}{d}\right) \tag{5}$$

In Eqs. 4 and 5, ε, the oscillation parameter, is given by

$$\varepsilon = \frac{1}{2\pi}\ln\left(\frac{1-\beta}{1+\beta}\right) \tag{6}$$

It is assumed that pure mode I is applied remotely. Hence, on the boundary $d = x = R$, $\overline{\psi}(R) = 0$, i.e. $K_{II}^{\infty} = 0$. According to Eq. 4, this leads to some mixed-mode at the crack tip as $\overline{\psi}(0) \neq 0$. Finally, the two elastic materials are modelled using 4 nodes plane-strain elements with reduced integration (CPE4R) while the cohesive zones are modelled using 4 nodes cohesive elements (COH2D4). Plane strain elements are used as plane strain state is found in DCB joints, except along the edges [47]. In addition, plane strain mode I fracture toughness is more critical than plane stress mode I fracture toughness.

2.2. Double cantilever beam model (DCB)

The double cantilever beam (Fig. 2b) consists of three layers: the two external ones correspond to the adherends of the joint while the internal layer is referred to as the interlayer. Both adherends are made of material 2 to limit the number of parameters, and to get rid of effects originating from dissimilar adherends such as the introduction of a slight mode II component at the crack tip [39]. The interlayer between the two material 2 adherends is made of material 1 that also fills the grooves. Indeed, in thermoplastic composite-metal joints, a thin thermoplastic layer can be found between the metal and the thermoplastic composite [6]. This interlayer has a thickness h_1, as defined in Fig. 2b. Preliminary results showed that this thickness does not influence the results if below 100 μm ($h_1/l_s^1 = 0.1$), while it is often limited to few microns in TPC-metal joints [6]. Both material 2 adherends have a thickness h_2. The grooves have a depth D, a length L and a spacing S, like for the SSY model. All materials are perfectly elastic with a Young's modulus E_i and a Poisson ratio ν_i. Similar to the previous model, two cohesive zones are inserted, detailed in Section 2.3., one along the interface and the other one in the thin layer made of Material 1. The two elastic materials are modelled using 4 nodes plane-strain elements with reduced integration (CPE4R) while the cohesive zones are modelled using 4 nodes cohesive elements (COH2D4). Plane strain elements are used as plane strain stress state is found in DCB joints [47]. Classically, a displacement boundary condition is applied at the beam ends as shown in Fig. 2b. However, owing to convergence issues resulting from snap-back instabilities, a control algorithm has been implemented, based on the one of Martinez-Paneda et al. [48]. These convergence issues are prevented by controlling a monotonically increasing variable during the loading history. This variable is the relative crack face displacement at the initial crack tip location as done by Segurado and Llorca [49], and Martinez-Paneda et al. [48]. The algorithm is detailed in Appendix A.

2.3. Cohesive zone models

The cohesive zone elements are inserted using zero-thickness cohesive elements (COH2D4), and using a linear traction separation law (TSL), shown in Fig. 2. The TSL is characterized by a cohesive strength σ_c, a critical opening displacement δ_c and a cohesive energy Γ_c, linked to each other via

$$\Gamma_c = \frac{\sigma_c \delta_c}{2} \tag{7}$$

Mode-mixity is considered but it is assumed that cohesive strength and energy are mode-independent and failure takes place when

$$\sqrt{\left(\frac{\delta^N}{\delta_c}\right)^2 + \left(\frac{\delta^T}{\delta_c}\right)^2} = 1 \tag{8}$$

where δ^N and δ^T are the normal and tangential opening displacement, respectively. Consequently, the interface cohesive zone is characterized by cohesive energy and strength Γ_c^i and σ_c^i while the cohesive zone inserted to model cohesive failure in Material 1 is characterized by Γ_c^1 and σ_c^1.

The increasing linear part of the cohesive zone law is characterized by a stiffness K_{coh}. Turon et al. did not find any influence for K_{coh} values larger than 10^4 MPa/mm [50]. In the present case, a stiffness value of 10^6 MPa/mm is used, although larger values were not found to change the results. The displacement corresponding to the attainment of the cohesive strength, for both cohesive laws, is lower than $0.05\delta_c$, for all investigated cohesive parameters.

Inserting cohesive elements results in a fracture length scale l_{cz} in the model. It is also referred to as the fracture process zone and corresponds to the region ahead of the crack over which the cohesive elements are damaged, i.e. softening part of the TSL, and is proportional to the characteristic length l_s. The characteristic length for cohesive failure in Material 1 [50,51], given by Eq. 9, is taken as the reference length in the model.

$$l_s^1 = \frac{\Gamma_c^1 E_1}{\sigma_c^1} \tag{9}$$

The fracture process zone length is given by $l_{cz} = Ml_s$, where M is a parameter that depends on the cohesive zone model and geometrical dimensions. For the most commonly used models in the literature involving purely elastic materials, Hilleborg's [52] model and Rice's [53] model, M is either equal or close to 1, implying $l_{cz} = l_s$. M is also affected by the model dimensions in terms of remaining ligament ahead of the crack tip [54], beam thickness in the case of delamination problem [55], and cohesive law shape [50]. Consequently, as l_{cz} might be influenced by the groove dimensions, the characteristic length l_s^1 is used as reference length.

The meshing algorithm depends on the characteristic length and is summarized in Fig. 3a. If the groove dimensions exceeds the characteristic length, the element size is equal to maximum one fifth of l_s, to avoid mesh-size dependency [50]. For groove dimensions lower than the characteristic length, 5 elements are inserted along the dimension of interest. If the aspect ratio of the elements surrounding the cohesive elements exceeds a value of 3, the length of the longest cohesive element is limited to 3 times the length of the smallest cohesive element. Mesh details for the SSY and DCB geometries are shown in Figs. 3b to 3e for $E_1/E_2 = 0.1$, $\Gamma_c^1/\Gamma_c^i = 10$, $\sigma_c^1/\sigma_c^i = 1$. This meshing algorithm was found to lead to mesh convergence. For some simulations (<1%), convergence was not achieved, but this could be solved by further refining the mesh. Typical meshes are shown in Fig. 3.

Finally, the failure mechanism taking place thus depends on E_1/E_2, Γ_c^1/Γ_c^i, σ_c^1/σ_c^i, D/l_s^1 and D/L for the SSY model. E_1, σ_c^1 and Γ_c^1 are fixed, while D, L, E_2, σ_c^i and Γ_c^i are varied to modify these ratios. Note that the σ_c^1/σ_c^i and Γ_c^1/Γ_c^i ratios investigated range between 1 and 10. To limit the number of variables and because it has been reported to not have an influence [9], the groove spacing S is not considered as a variable. For the DCB model, the additional variable is h_2. The material 1 interlayer thickness h_1 could be considered as well as a variable but its influence on the failure mechanism was found to be marginal. The failure mechanism is determined based on the crack path in the model. When a crack reaches a groove, cohesive failure is considered to take place if the cohesive elements corresponding to cohesive failure fail, while interface failure is considered if the cohesive elements located along the groove edges fail. Simulations are run for several Γ_c^1/Γ_c^i and σ_c^1/σ_c^i ratios to determine the transition curve between cohesive and interfacial failure. The full

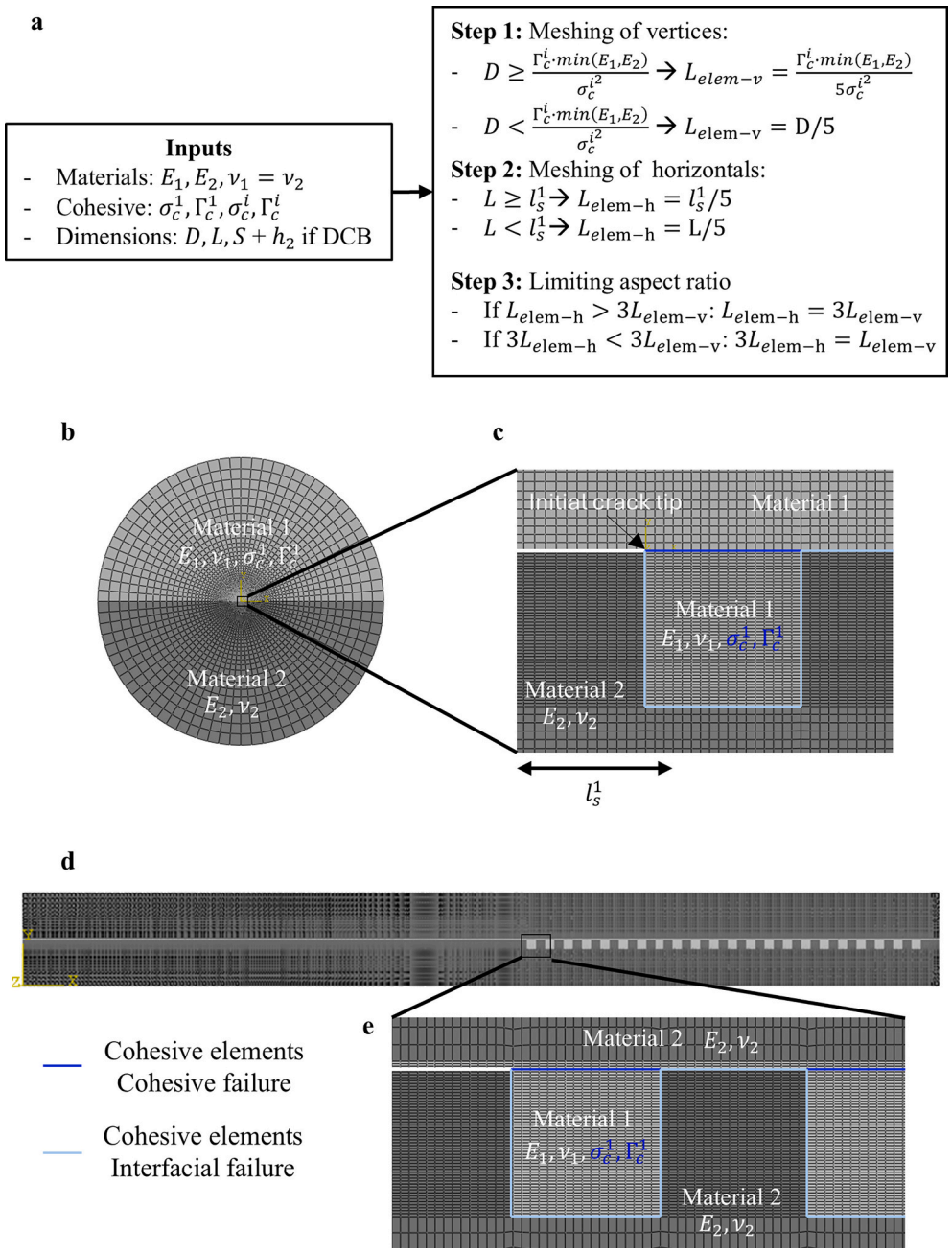

Fig. 3. a) Meshing algorithm to determine the element size depending on geometrical, material and cohesive parameters. b)-e) Mesh details for $E_1/E_2 = 0.1$, $\Gamma_c^1/\Gamma_c^i = 10$, $\sigma_c^1/\sigma_c^i = 1$, $D = W = S = l_s^1$ for b)-c) the SSY model and d)-e) the DCB model if $h_2 = 5l_s^1$.

workflow is shown in Supplementary Material 1.

2.4. Limitations of the model

In this study, several simplifying assumptions are made in terms of materials, geometry, loading and failure mechanisms.

First, the materials are assumed to be perfectly elastic, although thermoplastics and adhesives generally exhibit an elastoplastic behaviour. Plastic deformation at bimaterial interfaces can significantly alter the crack path compared to a purely elastic prediction, as shown by Tilbrook [56] compared to the elastic solution of Fleck et al. [57]. Incorporating plasticity would require additional parameters, such as the ratio between cohesive strength and yield strength [40], thereby increasing the number of variables.

Second, the context of the study is interface toughening between TPC and metals. In the study, the thermoplastic can be associated to material 1, which is considered homogeneous. However, in TPC–metal assemblies, processing conditions such as cooling rate can induce variations in crystallinity, leading to gradients in stiffness, strength and brittleness [58–60]. These property gradients, as well as potential crystallinity-dependent cohesive behaviour, are not captured by the present model.

Third, a single pattern design is considered, i.e. square grooves. Theses grooves exhibit 90° corner in order to neglect the influence of the radius of corner rounding on the failure mechanism taking place along the interface. In addition, statistical variability in the geometry arising from manufacturing is no considered.

Furthermore, perfect wetting and full filling of the grooves are assumed. In practice, groove filling depends on both geometry and the viscosity of the molten polymer, and partial filling may occur [13,32]. This aspect is briefly discussed in Appendix C.

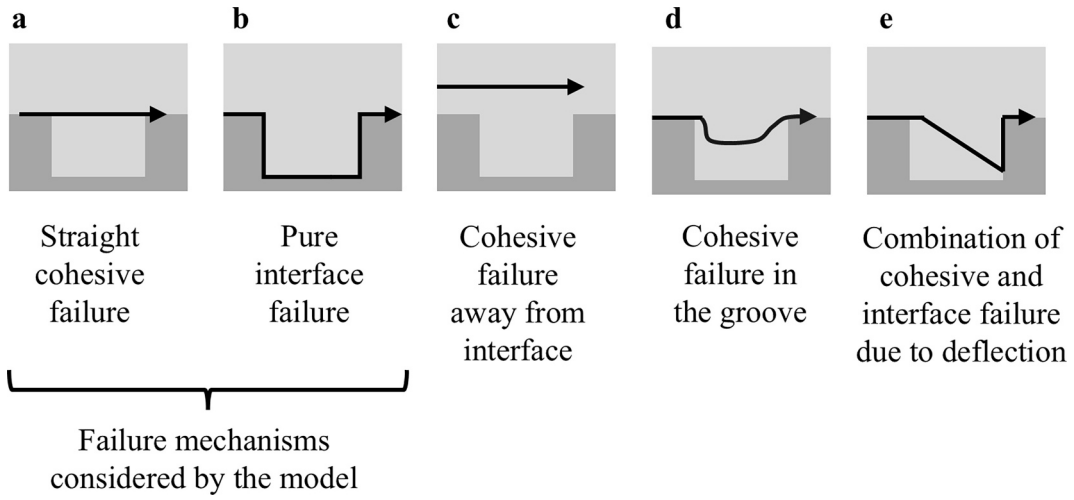

Fig. 4. Possible crack paths along patterned interfaces: a) cohesive failure, b) interfacial failure, c) cohesive failure in material 1 away from the interface, d) cohesive failure with crack deflection in the groove and e) combination of cohesive and interfacial failure. a) and b) are the only crack paths considered by the model.

In addition, crack propagation along the interface (Fig. 4b) and straight cohesive propagation into material 1 (Fig. 4a) are the only possible failure mechanisms. However, experimentally, other crack paths can also be observed [28], such as cohesive failure in material 1 away from the interface or in the groove, or a combination of cohesive and interfacial failure, as illustrated in Fig. 4c-e. Failure of grooves wall could also take place depending on S. Considering all these crack paths requires inserting cohesive elements between all continuum elements, significantly increasing the computational cost of the models, or using other modelling techniques such as the XFEM approach.

Finally, upon assembly, residual stresses develop in the assembly due to thermal expansion coefficient mismatch [61]. These stresses can modify the local mode-mixity, T-stress, and, consequently, the crack mechanism.

3. Results

The influence of material and cohesive properties on the failure mechanisms, i.e. cohesive or interfacial, is first investigated using the small-scale yielding model in order to eliminate the influence of the material 2 (adherends) bending stiffness inherent to the DCB geometry. Afterwards, the influence of the DCB geometry on the failure mechanisms is investigated. In both cases, the groove spacing S is kept constant, equal to $10l_s^1$, to limit the number of parameters. In addition, Kim et al. [9] did not find any influence of S on the failure mechanisms taking place along patterned interfaces.

Before discussing the results, a preliminary remark must be made regarding their presentation. The results are shown for several groove dimensions and elastic mismatches on graphs that depend on Γ_c^1/Γ_c^i and σ_c^1/σ_c^i. For each investigated condition, a curve delimiting the transition between the cohesive and interfacial failure mechanisms is shown. The curves exhibit a vertical asymptotic behaviour, as shown in Fig. 5, in agreement with the results of Parmigiani and Thouless [33]. This indicates that the failure mode is mainly governed by the cohesive strength ratio rather than by the toughness ratio. Cohesive failure takes place for combinations of Γ_c^1/Γ_c^i and σ_c^1/σ_c^i located at the left side of the transition curve. The more the curve is shifted towards the right side of the graph, the more cohesive failure is promoted, meaning that a larger contrast in cohesive strength between material 1 and the interface, i.e. large σ_c^1/σ_c^i value, is required to trigger crack deflection along the interface. The transition curves are defined by error bars owing to the uncertainty on the exact value of σ_c^i/σ_c^1 at which the transition takes place. Identifying this exact value is computationally demanding, and convergence issues often arise near the transition due to intense competition between the two mechanisms. Consequently, the error bar interval is generally set to 0.5, although in some cases it could be reduced to 0.25.

3.1. Small scale yielding model

The elastic mismatch between the materials on either side of the interface, quantified by the parameter α (Eq. 1), plays a significant role in governing the failure mechanism taking place along the interface [33]. Before investigating its effect, the influence of the groove depth D and length L is investigated in the absence of any elastic mismatch $\alpha = 0$, $E_1 = E_2$. In order to give an idea of the interface characteristic length with respect to the groove dimensions, light grey curves are shown on the graphs for constant values of the characteristic length scales ratio, l_s^i/l_s^1.

3.1.1. Influence of groove dimensions without elastic mismatch

The two important dimensions to investigate are the depth D and the length L of the groove. The results are respectively shown in Figs. 5 and 6.

- Influence of the groove depth D

The first dimension to investigate is the groove depth D as increased roughness depth is known to promote mechanical interlocking [7,8]. Fig. 5 shows the influence of the depth normalized by the reference characteristic length l_s^1. The length and the spacing between the groove are fixed to $L = S = 10l_s^1$.

Fig. 5a shows the influence of the depth, the cohesive strength ratio and the toughness ratio on the transition between the cohesive and the interfacial failure mechanisms. For a deep groove (red curve in Fig. 5a), i.e. $D/l_s^1 = 10$, the results are similar to those of Parmigiani and Thouless [33], with small differences due to the different problem geometry. Fig. 5a shows that decreasing the groove depth to $D/l_s^1 = 0.1$ (green curve) promotes crack deflection along the interface as the curves tend to be shifted towards the left, to lower strength ratios. Consequently, crack deflection occurs even if the interface is almost as strong as material 1, i.e. $\sigma_c^1/\sigma_c^i \sim 1$, for shallow grooves, while for deep grooves the interface can be significantly less strong and tough than material 1, i.e. large σ_c^1/σ_c^i and Γ_c^1/Γ_c^i values, and crack deflection will still be observed.

In the case of a deep groove, the stress singularity developing ahead of the crack tip remains confined to the upper portion of the groove.

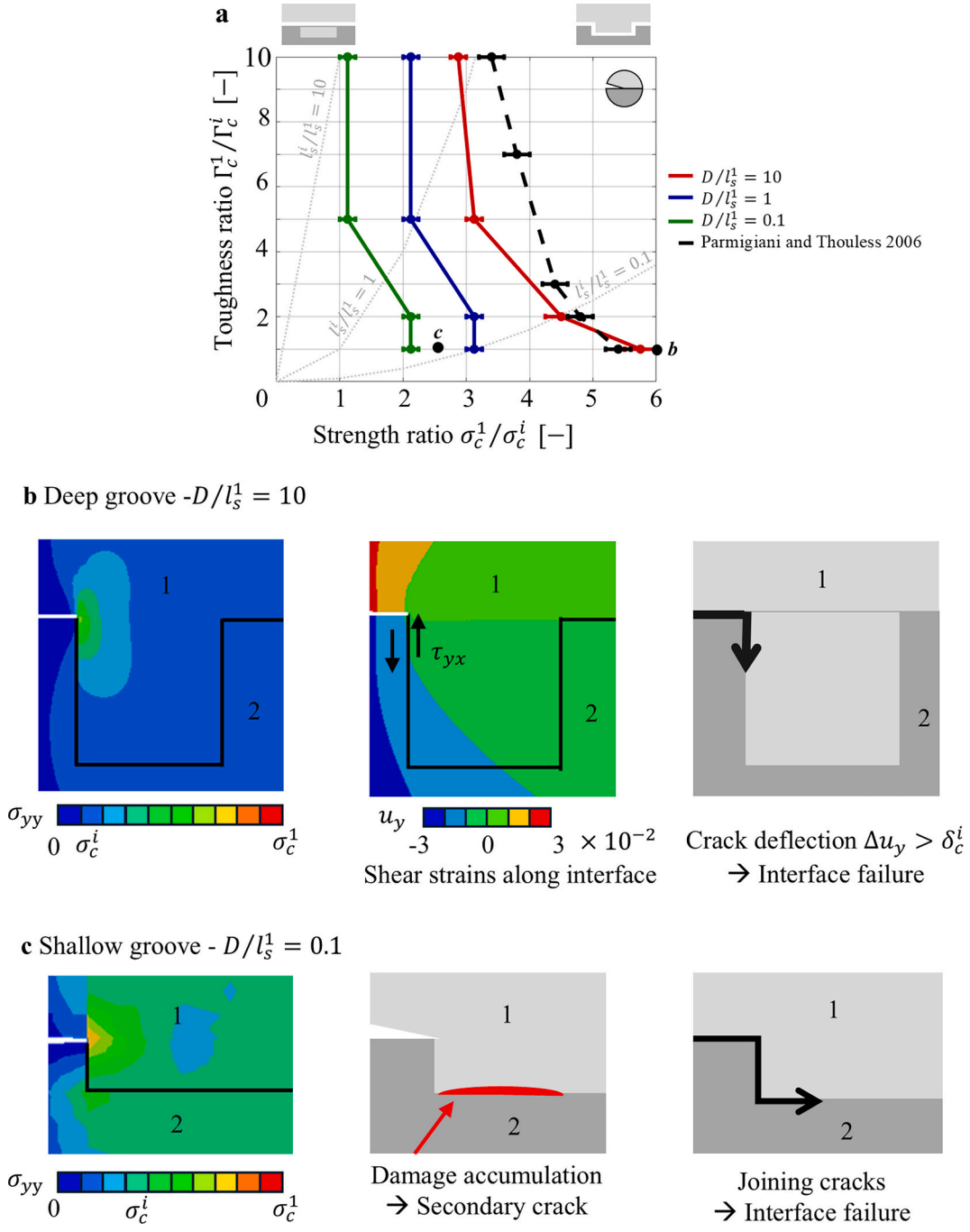

Fig. 5. a) Influence of the groove depth D on the transition between cohesive (left of the curve) and interfacial failure (right of the curve) depending on Γ_c^1/Γ_c^i and σ_c^1/σ_c^i. Schematic representations of the deflection mechanism associated with interfacial failure and representative Abaqus simulations snapshots just before failure for b) a deep groove and c) a shallow groove. For b) $\sigma_c^1/\sigma_c^i = 6$ and $\Gamma_c^1/\Gamma_c^i = 1$, and for c) $\sigma_c^1/\sigma_c^i = 2.5$ and $\Gamma_c^1/\Gamma_c^i = 1$. No elastic mismatch is considered in both cases and $L = 10l_s^1$.

However, the deformation field surrounding the crack tip generates significant shear stresses along the interface, as illustrated in Fig. 5b. Shear stresses along the groove edge results from differences in displacements between material 1 and material 2. Deflection only takes place when relative displacement between the two sides of the vertical interface exceeds δ_c^i. Increasing Γ_c^1/Γ_c^i is similar to decreasing Γ_c^i and thus reducing the critical opening displacement of the interface δ_c^i. The maximum deformations around the crack tip is dictated by Γ_c^1 and the material properties. If Γ_c^i decreases, lower deformations are required to result in crack deflection, and, consequently, a higher Γ_c^1/Γ_c^i promotes interfacial failure.

Opposite, a shallow groove tends to promotes crack deflection. As shown in Fig. 5c, stress singularity extends to the bottom interface of the groove. Under certain conditions, this leads to stresses exceeding σ_c^i along that interface resulting in damage accumulation. This leads to the nucleation of a secondary crack interacting with the main crack. This secondary crack attracts the main crack, forcing its deflection along the interface.

To conclude, crack deflection takes place either (1) when high shear stress develop along the interface due to crack tip strain field or (2) when normal stresses are generated at the bottom face of the groove due to

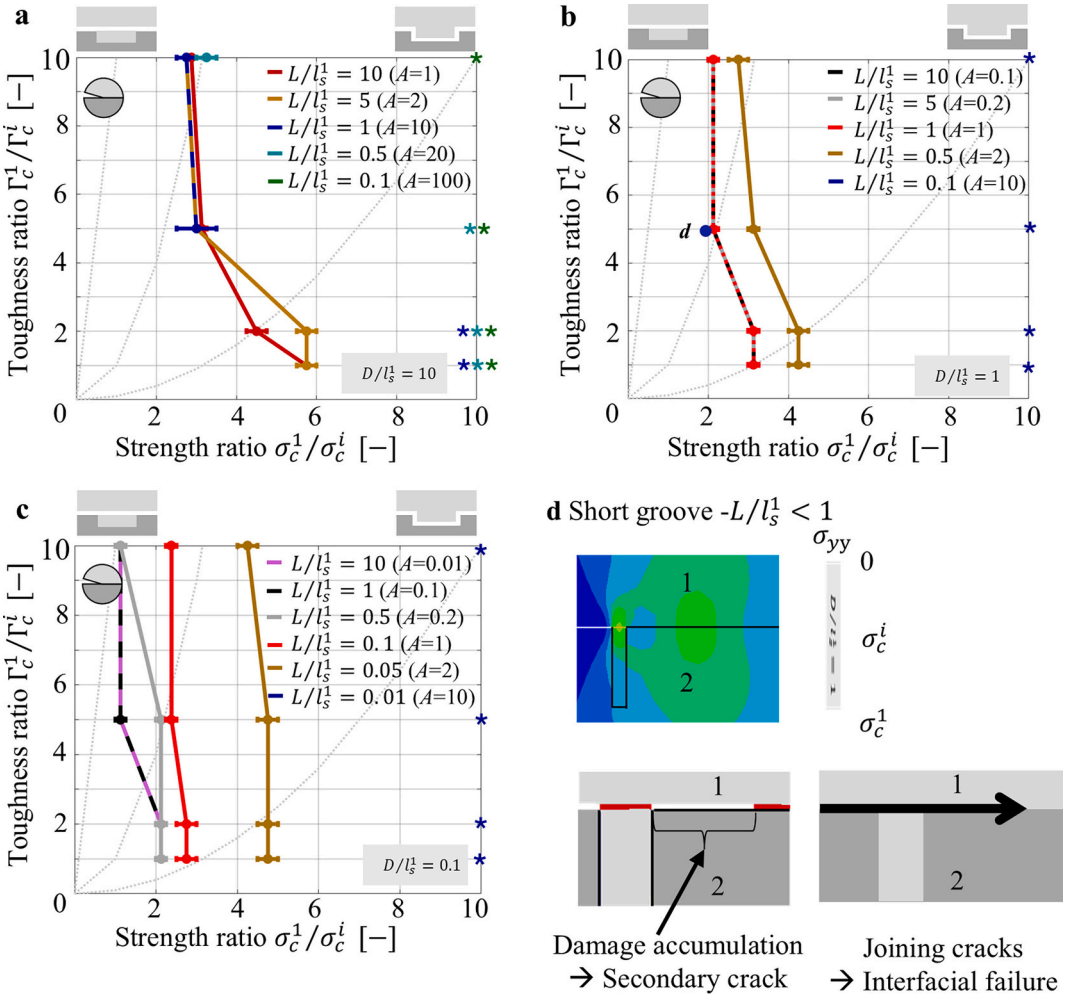

Fig. 6. Influence of the groove length L on the transition between cohesive and interfacial failure depending on cohesive energy ratio Γ_c^1/Γ_c^i and cohesive strength ratio σ_c^1/σ_c^i for a) a deep groove $D/l_s^1 = 10$, b) an intermediate groove depth such that $D/l_s^1 = 1$ and c) a shallow groove $D/l_s^1 = 0.1$ d) Abaqus simulation snapshots, representative of the cohesive failure mechanism for a short groove ($A = D/L \geq 10$, $D = l_s^1$, $\sigma_c^1/\sigma_c^i = 2$ and $\Gamma_c^1/\Gamma_c^i = 5$). No material mismatch is considered, hence $E_1 = E_2$.

crack tip stress singularity.

- Influence of the groove length

The influence of the groove length L on the failure mechanism is shown in Fig. 6. A combined effect of the groove length L and the groove depth D is observed. A decrease in groove length tends to prevent interfacial failure (shifting of the curves towards the right). However, for a given length L, the position of the transition curve also depends on the groove depth as observed when comparing Fig. 6a, b and c. Two cases must be therefore distinguished. The first one corresponds to deep grooves such that $D > l_s^1$. In this case, the transition curves tend to overlap each other for grooves aspect ratio, defined by $A = D/L$, lower than 10. This corresponds to groove length L longer than l_s^1. For higher aspect ratios, cohesive failure is the only observed failure mechanism for cohesive strength ratios σ_c^1/σ_c^i lower than 10. The second case corresponds to groove with a depth lower or equal to the characteristic length l_s^1. In that case, the transition curve moves to the right, indicating a preference for cohesive failure, when the groove aspect ratio exceeds a value of 1. When the aspect ratio is about 10, no deflection is predicted by the simulations for $\sigma_c^1/\sigma_c^i \leq 10$. The conditions for which no interfacial failure is observed for $\sigma_c^1/\sigma_c^i \leq 10$ are highlighted by stars in Fig. 6. To conclude, the finite element model only predicts cohesive failure for any values of σ_c^1/σ_c^i lower than 10 if the groove length is lower than the characteristic length, i.e. $L < l_s^1$, and if the aspect ratio is at least equal to 10, i.e. $A \geq 10$.

For short grooves, i.e. $L < l_s^1$, the phenomenon resulting in cohesive failure is depicted in Fig. 6d. The stress field generated by the presence of the crack extends beyond the end of the groove. If the stress at this location exceeds σ_c^i, damage accumulates along the interface, nucleating a secondary crack on the same plane as the main crack. These cracks interact together, forcing the main crack to propagate straight through material 1. However, the groove length at which this happens also depends on the depth as there is a competition between this mechanism promoting cohesive failure and the mechanism promoting deflection that depends on the groove depth.

To conclude, to promote cohesive failure, groove depth and length are important. They can be linked to each other through the aspect ratio A. It is found that deeper and shorter grooves tend to promote cohesive failure, and to be more specific, cohesive failure is always observed when $\sigma_c^1/\sigma_c^i \leq 10$ if $A = D/L$ is larger than 10, and L is smaller than l_s^1. Cohesive failure is believed to be the toughest mechanism and should thus be favored. Rougher surfaces, corresponding to deep grooves in the present case, are reported to promote cohesive failure owing to mechanical interlocking [8]. However, the present results show that not only roughness, and thus depth, is important, but also the groove length,

which corresponds to the autocorrelation length of the surface roughness. This last parameter has received comparatively less attention in the literature, yet the present study indicates that it influences mechanical interlocking.

3.1.2. *Influence of the elastic mismatch*

In adhesive joints and thermoplastic-metal joints, the grooves are filled with adhesive or thermoplastic respectively, characterized by a lower Young's modulus than the metal. There is thus an elastic mismatch. At bimaterial interfaces, the crack tip stress field is affected by the elastic mismatch which results into the development of shear stresses if a mode I loading is applied at the outer boundary of the SSY model [62]. This results in some mode-mixity at the crack tip, influencing the toughness and the failure mechanisms. The influence of the elastic mismatch on the transition between cohesive and interfacial failure is investigated and the results are shown in Fig. 7 for D/l_s^1 ratios equal to 10, 1 and 0.1, while the groove length and spacings are fixed to $L = S = 10l_s^1$ to limit the number of variables.

In Fig. 7a, b and c, the black curve is the reference curve corresponding to a case without any elastic mismatch. Material 1 being stiffer than material 2 ($\alpha < 0$, dashed curves in Fig. 7) results in a shift of the curve towards the left. Hence, a stiffer material 1 than material 2 tends to promote deflection. On the opposite, a softer material 1 tends to prevent deflection as the curves are shifted towards the right. The higher the elastic mismatch (larger $|\alpha|$), the more the transition limit is influenced, in agreement with the results of Parmigiani and Thouless [33]. However, comparing Figs. 7a to 7c, it is also observed that the shallower the groove, the less the elastic mismatch tends to have an influence on the transition between the two failure mechanisms as the curves tend to overlap each other.

Fig. 7d shows the stress field ahead of the crack tip for $\alpha < 0$, $\alpha = 0$ and $\alpha > 0$. A rotation of the stress field is observed for $\alpha \neq 0$, resulting in a mode II component different from zero, as illustrated in Fig. 7d. These stress distributions have an influence on the failure mechanism. For $\alpha > 0$, the vertical edge of the groove is under compression, preventing deflection as interfacial failure is only caused by shear. Opposite, when

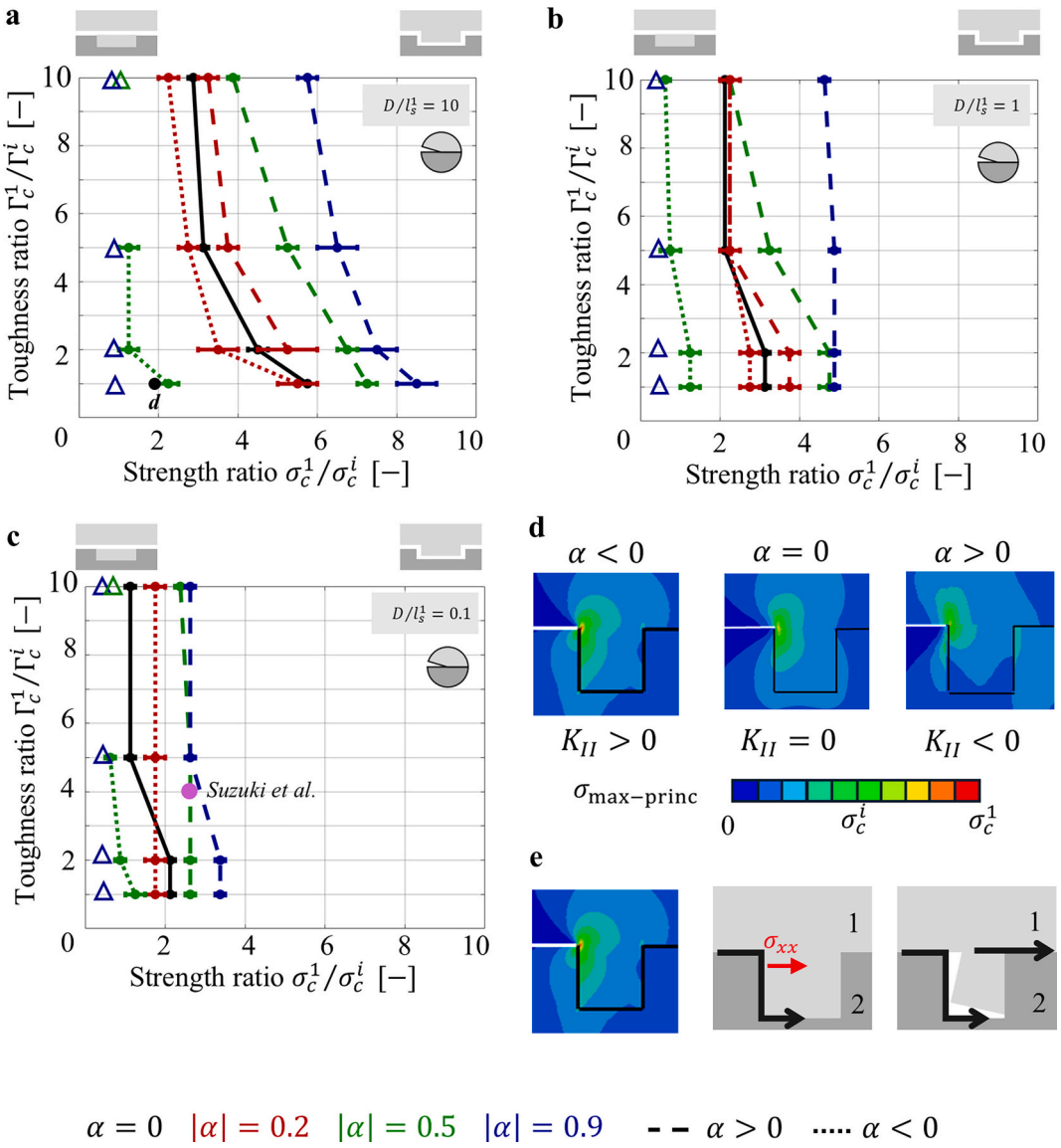

Fig. 7. Influence of the elastic mismatch quantified by α (Eq. 1) for three different depths: a) $D = 10l_s^1$ (deep), b) $D = l_s^1$ and c) $D = 0.1l_s^1$ (shallow).The length L of the groove is set to $10l_s^1$. The triangles indicate that interfacial failure followed by "cohesive failure due to constraint" takes place for $\sigma_c^1/\sigma_c^i < 1$, and the exact transition value could not be determined. d)Abaqus snapshots of the maximum principal stress-field ahead of the crack tip depending on α ($D = L = l_s^1$, $\sigma_c^1/\sigma_c^i = 2$ and $\Gamma_c^1/\Gamma_c^i = 1$, $\alpha = -0.5, 0$ and 0.5. e) Schematic representation of the cohesive failure due to constraint mechanism if material 1 is stiffer than material 2, i.e. $\alpha < 0$.

$\alpha < 0$, this edge is loaded under tension as shown in Fig. 7e, promoting interfacial failure. However, once interfacial failure takes place, the motion of the groove material (material 1) is prevented by the surrounding material (material 2). Hence, full interfacial failure cannot take place, and a second crack starts in material 1 and join the initial crack tip. This mechanism is referred to as *"cohesive failure due to constraint"* and has already been reported by Yukimoto et al. [27] under mode II loading.

Elastic mismatch can influence the crack path selection. For example, when cohesive failure takes place, this can lead to slight deflection away or inside the groove, as illustrated in Fig. 8. Indeed, a crack propagating close to a bimaterial interface tends to propagate towards the interface if propagating in the stiffest material, or away of the interface if propagating in the most compliant material [57,63–65]. Such cracks paths are not considered in the current model as inserting cohesive elements between all continuum elements would significantly increase the computational cost. However, this could be analyzed by looking at the hoop stresses [66] ahead of the crack tip or with the XFEM method.

To conclude, the elastic mismatch influences the failure mechanism taking place along the interface. A more compliant material 1 tends to promote cohesive failure, opposite to a stiffer material 1. This results from the stress-state at the crack tip. The stress-state also depends on the geometry of the sample and on the applied loading. Consequently, this must be considered to maximize the overall joint toughness.

3.1.3. Influence of mode-mixity

The influence of mode-mixity on the transition between cohesive and interfacial failure is investigated. Indeed, thermoplastic-metal interfaces generally exhibit a pronounced dependence on fracture mode, with mode II fracture toughness, i.e. Γ_{IIc}, often exceeding mode I toughness, i.e. Γ_{Ic}, a trend widely documented in mixed-mode studies of laminated and hybrid material systems where in-plane shear requires greater energy dissipation than opening-mode fracture [67,68]. Despite this, joints frequently possess higher tensile strength than shear strength. Consequently, transition between cohesive failure and interfacial failure cannot be understood from toughness ratios (Γ_{IIc}/Γ_{Ic}) alone as the relative cohesive strengths in shear and tension (τ_c/σ_c) might also play a significant role.

Fig. 9a investigates the combined influence of mode-mixity, elastic mismatch and groove depth for an aspect ratio equal to 1 and $\Gamma^1_{Ic}/\Gamma^i_{Ic} = 10$. The toughness ratio Γ_{IIc}/Γ_{Ic} is set to 10 for both the interface and material 1 while keeping $\tau_c = \sigma_c$. No influence on the cohesive strength ratio leading to interfacial failure is found for $D = L = l^1_s$. This is attributed to the crack path being governed by tensile loading at the bottom of the groove. In contrast, when $D = L = 10l^1_s$, variations in mode-mixity induce clear shifts in the transition behaviour for $\alpha > 0$. Under these conditions, the groove edges experience predominantly shear loading. Consequently, increasing mode II toughness raises the critical displacement required to drive interfacial crack propagation, thereby promoting cohesive failure. For $\alpha < 0$, there is no change as the groove vertices experience tensile stresses as shown in Fig. 7e. This agrees with the trends found by Parmigiani and Thouless [33].

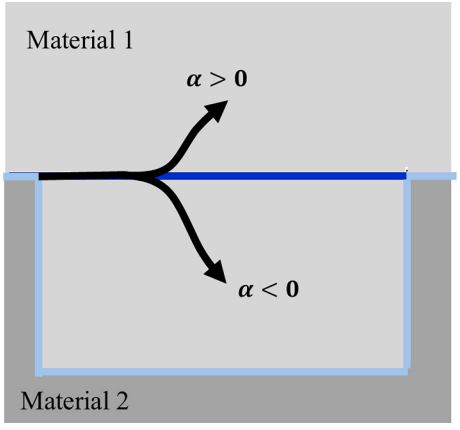

Fig. 8. Potential crack paths observed when cohesive failure takes place due to the elastic mismatch between materials 1 and 2. The blue lines correspond to the crack paths imposed by the cohesive elements in FE the model. (For interpretation of the references to colour in this figure legend, the reader is referred to the web version of this article.)

The combined influence of aspect ratio and mode-mixity for $D = l^1_s$ and $\alpha = 0$ is investigated in Fig. 9b. For an aspect ratio of 1, mode-mixity does not influence the failure mechanism taking place, while a rightward shift for an aspect ratio of 2 is found. Consequently, mode-mixity can influence the aspect ratio for which cohesive failure is always observed if σ^i_c/σ^1_c is larger than 10. This critical aspect ratio can decrease, but the accurate value depends on other groove dimensions and elastic mismatch.

Finally, when Γ_{IIc}/Γ_{Ic} is set to unity and the cohesive strength ratio is set to $\tau_c/\sigma_c = 1/\sqrt{3}$. In Fig. 9c, the transition curve is shifted to the left, indicating that decreasing the shear cohesive strength favours interfacial failure. This outcome aligns with cohesive zone modelling studies of polymer composite interfaces, which report that reduced shear strength significantly weakens resistance to mixed-mode interfacial cracking [69]. Notably, when the results are expressed in terms of τ^i_c/σ^1_c, the curves collapse as the ratio between the blue and red dots in Fig. 9c is about $\sqrt{3}$, underscoring that the ratio between normal and shear cohesive strengths predominantly governs the onset of interfacial failure.

To conclude, the results show that mode-mixity influences the point at which failure transitions from cohesive to interfacial, but only under conditions where the interface is primarily subjected to shear. When the failure path is governed by tensile fields, such as at the bottom of shallow grooves, the effect of mode-mixity becomes negligible. Conversely, in geometries or loading conditions that create shear-dominated regions, higher mode II toughness promotes cohesive failure, whereas reduced shear cohesive strength promotes interfacial failure. Mode-mixity can thus influence the critical aspect ratio for which cohesive failure is always observed for $\sigma^1_c/\sigma^i_c \geq 10$. Mode-mixity in terms of cohesive energy tens to decrease this ratio while mode-mixity in terms of cohesive strength tens to increase it.

3.1.4. Double cantilever beam model

The mode I fracture toughness of interfaces and joints is often determined using the double cantilever beam configuration. Mode I opening of the crack is induced by bending the DCB arms. In the present study, the total deflection of the beam depends on the crack length, the interface fracture toughness, the material 2 thickness h_2, and the material 2 Young's modulus E_2. Bending also results in horizontal strains, ε_{xx} given by

$$\varepsilon_{xx} = \sqrt{\frac{12\Gamma^1_c}{E_2 h_2}} \tag{10}$$

- Influence of material 2 thickness and properties

The influence of the material 2 thickness h_2 on the failure mechanism is shown in Fig. 10. Again, the failure mechanism depends on Γ^1_c/Γ^i_c and σ^1_c/σ^i_c. As for the SSY model, the cohesive strength ratio σ^1_c/σ^i_c is the cohesive parameter influencing the transition between the two failure mechanisms. In Fig. 10, the groove depth and length are kept constant such that $D = L = l^1_s$, while the groove spacing is fixed to $S = 10l^1_s$. It is found that increasing the thickness, h_2, prevents crack deflection along the interface as the transition curve is shifted towards the right side of the graph in Fig. 10. This indicates that the DCB geometry influences the observed failure mechanisms along the patterned interfaces. Referring

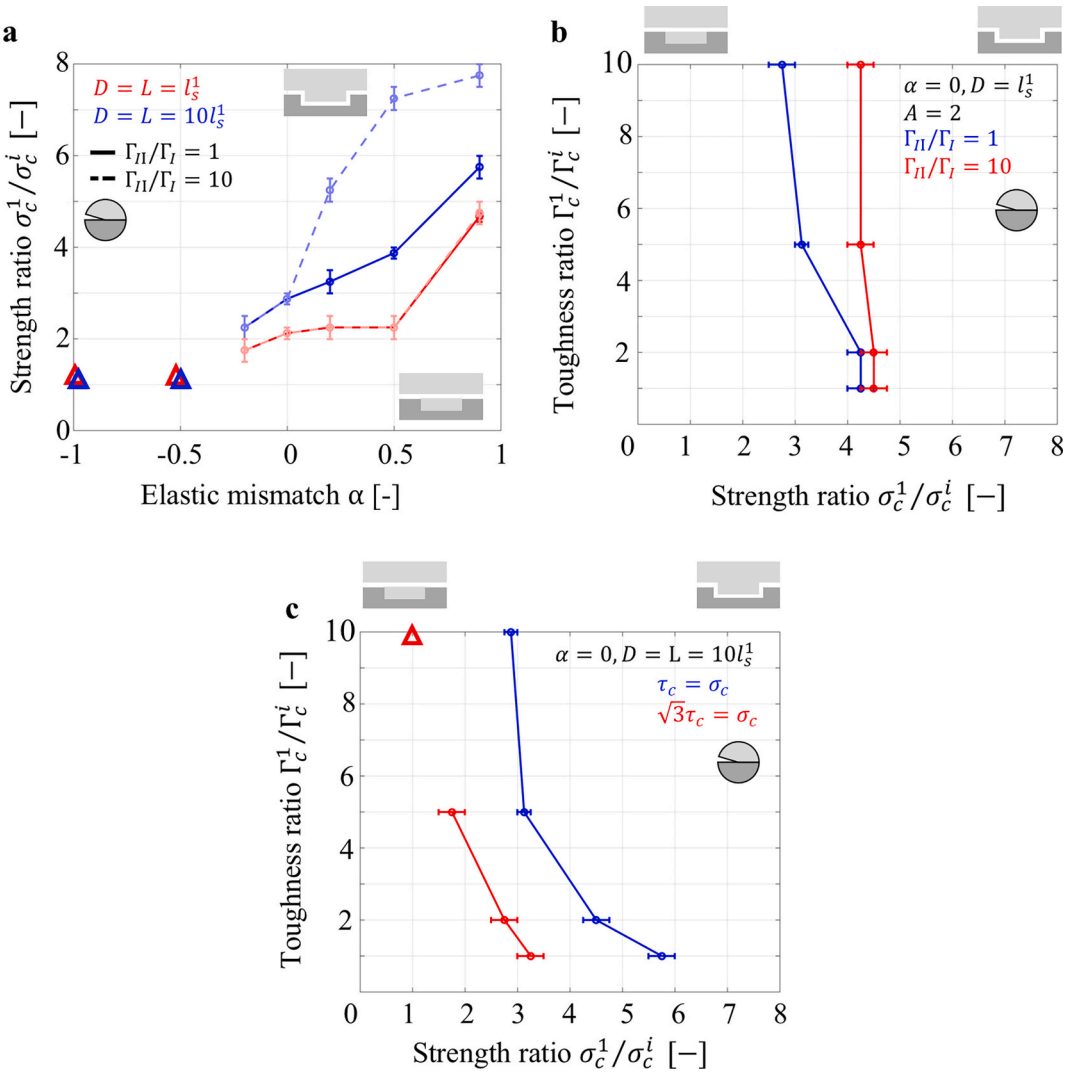

Fig. 9. Influence of mode-mixity on the transition between the mechanisms determined with the SSY model. a) Influence of mode-mixity depending on α for $D = L = l_s^1$ and $D = L = 10l_s^1$ for $\Gamma_{Ic}^1/\Gamma_{Ic}^i = 10$. Γ_{IIc}/Γ_{Ic} is set to 10, and $\tau_c = \sigma_c$. b) Influence of mode-mixity on the transition curve for $\alpha = 0, D = l_s^1$ and A = 2. Γ_{IIc}/Γ_{Ic} is set to 10, and $\tau_c = \sigma_c$. c) Influence of shear to normal cohesive strength ratio for $D = L = 10l_s^1$ and $\alpha = 0$. τ_c/σ_c is set to $1/\sqrt{3}$ and Γ_{IIc}/Γ_{Ic} to 1. Triangles indicate that for a strength ratio about 1, interfacial failure is observed.

to Eq. 10, decreasing material 2 thickness increases the bending strains and, consequently, the tensile stress acting along the groove vertices, favoring the opening of the cohesive elements located along that interface, promoting interfacial failure. This agrees with Fig. 10.

The material 2 Young's modulus E_2 also influences the bending strains close to the groove vertices. Its influence is investigated in Fig. 11. If E_2 increases, while E_1 is kept constant, cohesive failure is promoted if $\Gamma_c^1/\Gamma_c^i < 5$, as shown in Fig. 11a. However, the Young's modulus does not seem to have an effect on the transition between the cohesive and interfacial failure mechanisms for large toughness differences, $\Gamma_c^1/\Gamma_c^i \geq 5$. As E_1 is fixed, α increases if E_2 increases, which can influence the results as previously observed. In Fig. 11b, α is kept constant, equal to 2/3, while E_1 and E_2 are varied. A limited influence of the Young's modulus is then found. Comparing Fig. 11a and b suggests that the influence of the Young's modulus on the failure mechanism originates from the change in elastic mismatch. The larger the elastic mismatch, the more cohesive failure is promoted, in agreement with the results of the SSY model.

Eq. 10 indicates that increasing h_2 and E_2 results in lower bending strains ε_{xx}. The bending strains act as tensile strains along the groove edge, opening the cohesive elements located along the vertices. The higher the bending strains, the higher the tensile stresses acting along the groove vertices, which are no longer only subjected to pure mode II. Consequently, interfacial failure is promoted. It is expected to observe a similar influence of E_2 and h_2 on the results as $\varepsilon_{xx} \propto (E_2 h_2)^{-0.5}$. If only bending strains matter, doubling E_2 is expected to have the same influence as doubling h_2. However, this is not observed when comparing Figs. 10 and 11a. Hence, it can be concluded that, for fixed groove dimensions, the thickness of material 2 has a stronger influence on the failure mechanism than its Young's modulus. An hypothesis of this stronger influence of h_2 is that as h_2 increases, D/h_2 decreases and that this last ratio influences the failure mechanism. Whether or not D/h_2 influences the failure mechanism will be investigated in what follows.

- Influence of the groove depth

The influence of the groove depth is shown in Fig. 12a and b. The SSY model predicted an influence of the groove depth, with deeper grooves promoting cohesive failure. Opposite to the results of the SSY model, deeper grooves tend to promote interfacial failure when the DCB geometry is considered, as shown in Fig. 12a. As the depth of the groove decreases, cohesive failure is promoted, shifting the transition curve

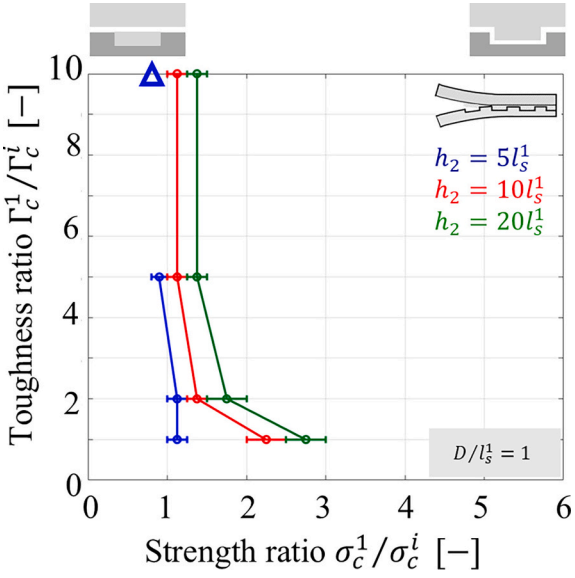

Fig. 10. Influence of a) material 2 thickness on the failure mechanisms depending on Γ_c^1/Γ_c^i and σ_c^1/σ_c^i, with D = L = l_s^1. The triangles indicate that interfacial failure followed by "cohesive failure due to constraint" takes place for σ_c^1/σ_c^i<1, and the exact transition value could not be determined.

towards the right in Fig. 11a. However, this shift is less marked than for the SSY model. Fig. 12b shows the influence of the depth normalized by the beam thickness. For $D/h_2 = 0.2$, increasing the beam thickness results in a slight promotion of cohesive failure as the curve is slightly shifted towards larger σ_c^1/σ_c^i values. However, for $D/h_2 = 0.05$, there is no clear trend. Indeed, the curves more or less overlap. At large toughness differences, thinner material 2 adherends tend to slightly promote cohesive failure compared to a thicker material 2 adherends. However, when the interface and material 1 are characterized by similar toughness, a thicker material 2 adherend promotes cohesive failure. For a given D/h_2, the thicker material 2, the deeper the groove. These results highlight the fact that there is competition between cohesive failure promoted by deep grooves (see section 3.1.1) and interface tensile stresses resulting from material 2 bending.

Increasing D/h_2 promotes interfacial failure. Simulations show that the deeper the groove for a given material 2 thickness, the higher the bending strains for given applied load and displacement. The situation can be seen as a partly built-in beam. The material 2 adherend is built-in only over a portion $1 - D/h_2$ of its thickness. Appendix B shows that the smaller the built-in part, and thus the higher D/h_2, the higher the bending strains. Shallower grooves also tend to promote deflection due to crack tip stress field interaction with the interface at the bottom of the groove as explained in Section 3.1.1. Hence, for any beam thickness h_2, there is a depth D promoting cohesive failure which depends on the D/h_2 effect and on the depth effect explained in Section 3.1.1. The thicker material 2, the deeper the optimal groove and the more cohesive failure is promoted.

- Influence of the groove length

As for the SSY model, the influence of the groove length L is investigated. The groove depth, D, is kept constant equal to l_s^1, while the beam thickness is varied. Fig. 13 shows that, similar to the SSY model, cohesive failure is promoted by shorter grooves. In addition, interfacial failure is no longer observed once the groove aspect ratio, $A = D/L$, is larger or equal to 10. Again, cohesive failure is observed for short grooves when the stress-field induces damage ahead of the crack tip as illustrated in Fig. 6d. It is important to note by comparing Fig. 13a and b that the material 2 thickness also has an influence on the critical aspect ratio above, which cohesive failure is always observed. Indeed, for a thin material 2 adherend (Fig. 10a), interfacial failure is still observed for large toughness ratios when σ_c^1/σ_c^i is larger than 7 (blue points), while cohesive failure is reported for the same groove geometry and the same properties for a thicker material 2 adherend (Fig. 13b – blue stars). This means that for thin material 2 beams, a higher groove aspect ratio D/L is required to ensure cohesive failure.

To conclude, the DCB model showed that the loading configuration influences the failure mechanisms taking place along a patterned interface. Material 2 bending promotes interfacial failure as it induces tensile stresses along the groove edge. Consequently, the deeper the groove, the more interfacial failure is promoted, opposite to the results of the SSY model. This effect depends on D/h_2. Shallower grooves can promote cohesive failure but below a certain depth, interfacial failure is again promoted as observed with the SSY model. Finally, cohesive failure is promoted when the groove aspect ratio exceeds a value of 10, as observed for the SSY model.

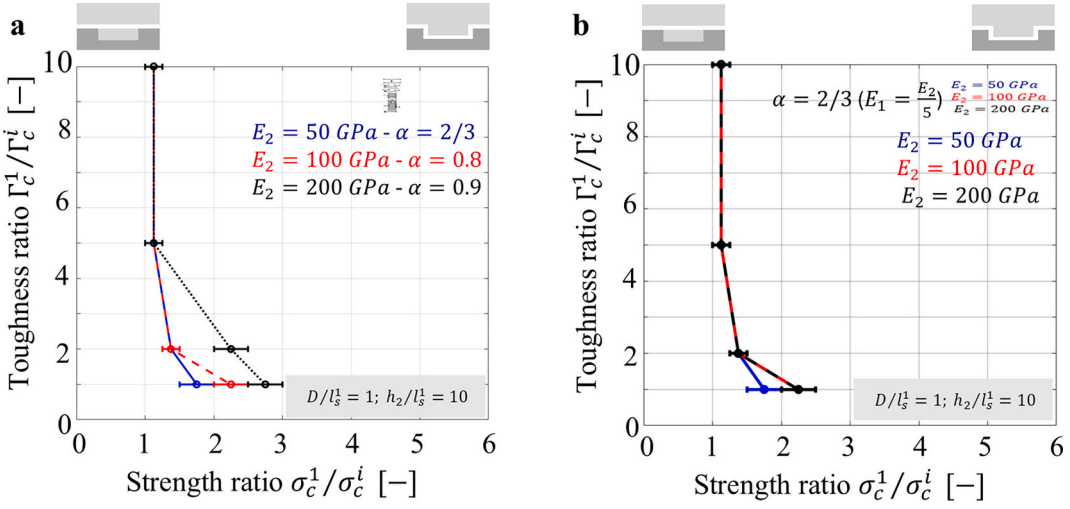

Fig. 11. Influence of material 2 Young's modulus on the failure mechanisms depending on Γ_c^1/Γ_c^i and σ_c^1/σ_c^i, with D = L = l_s^1. a) Fixed E_1, while E_2 and α vary. b) Fixed α, while E_1 and E_2 vary.

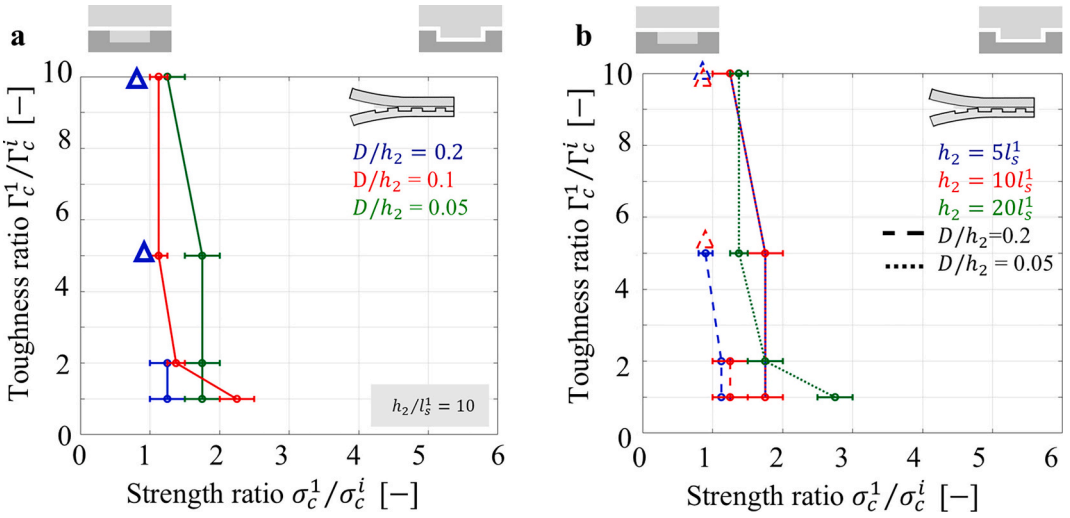

Fig. 12. Influence of the groove depth to material 2 thickness ratio D/h_2 on the transition between the cohesive failure to interfacial failure mechanism for a) material 2 thickness h_2 to $10l_s^1$ and b) varying material 2 thickness h_2, but constant D/h_2 ratios fixed to 0.2 and 0.05. The groove length is fixed to $L = l_s^1$. The triangles indicate that interfacial failure followed by "cohesive failure due to constraint" takes place for $\sigma_c^1/\sigma_c^i<1$, and the exact transition value could not be determined.

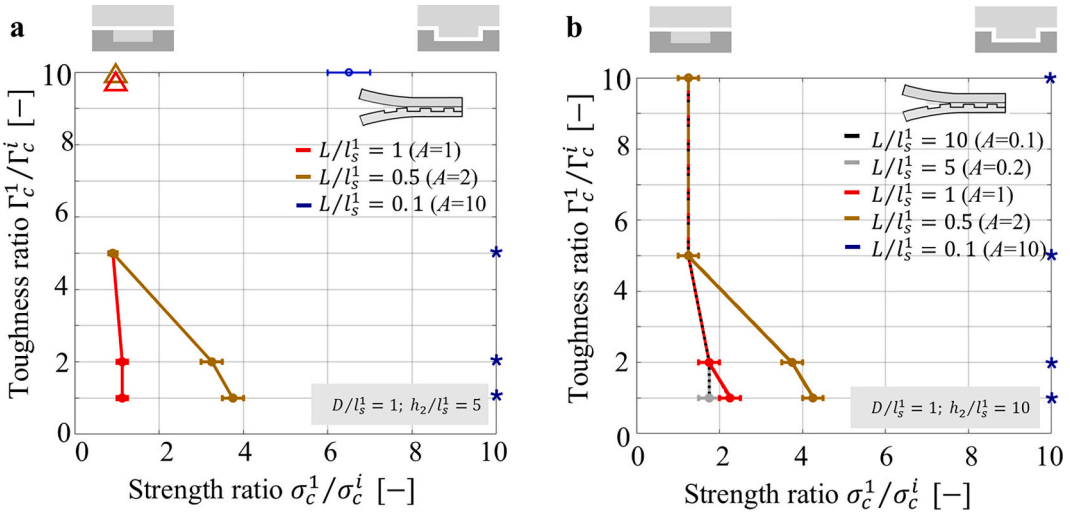

Fig. 13. Influence of the groove length L for the DCB model, with depth set to $D = l_s^1$ and groove spacing S equal to $10l_s^1$, depending on the cohesive energy ratio Γ_c^1/Γ_c^i and the cohesive strength ratio σ_c^1/σ_c^i for of a) a thin material 2 layer such that its thickness is $h_2 = 5l_s^1$ and b) a thick material 2 layer such that its thickness is $h_2 = 10l_s^1$. The elastic mismatch between material 1 and material 2 is set to $\alpha = 2/3$. Triangles indicate that crack deflection along interface is observed for these values, while * mean that only cohesive failure is observed.

4. Discussion

4.1. Model validation

The developed finite element model is compared to previous results concerning crack deflection at an interface and to experimental results obtained for adhesive joints and bimaterial interfaces.

Parmigiani and Thouless [33] developed a model predicting whether a crack deflects along an interface or penetrates into the adjacent material, depending on the cohesive strength and fracture toughness of the second material and of the interface. Their configuration differs from the present one: in their case, the crack first propagates through a block of material A before reaching the A-B interface, and if deflection occurs, it can proceed both upwards and downwards. In contrast, in the present work the crack propagates along the A-B interface before reaching a block of material B, and can only deflect downwards. Parmigiani and Thouless reported a stronger influence of the cohesive strength ratio than of the toughness ratio, with an asymptotic trend for large toughness ratios. Similar observations are made here. For $\alpha = 0$, the results of Parmigiani and Thouless are compared to the present results if $D = L = 10l_s^1$ in Fig. 3. For toughness ratios below 2, the transition between mechanisms occurs at similar strength ratios, while differences appear for larger toughness ratios. These discrepancies likely stem from differences in model configuration. They also found that increasing the characteristic length relative to the model dimensions promotes penetration, corresponding in the present notation to decreasing groove length L, which indeed promotes cohesive failure. Finally, they showed that crack penetration, equivalent here to cohesive failure, is favored by minimizing the elastic mismatch magnitude, $|\alpha|$, when toughness is mode-independent. However, if mode II toughness is significantly higher than mode I toughness, increasing α, and thus having material B significantly more compliant than material A promotes crack

penetration. This agrees with the actual results as it is found that cohesive failure is promoted if the grooves are filled by a more compliant material.

The finite element results can also be compared to experimental data found in the literature. Several researchers investigated interface toughening through groove patterning using lap-shear tests [9–15]. However, these results cannot be directly compared to DCB configurations because the loading mode alters the stress state. For example, Akman et al. [22] reported maximum shear strength for grooves with A $\approx$ 5, while lower aspect ratios (A $<$ 1) promoted interfacial failure. Similarly, Liu et al. [15] observed interfacial failure for A = 0.5 and cohesive failure for A $\approx$ 1, despite shallow grooves. These trends agree qualitatively with the present findings as higher aspect ratios promote cohesive failure, but the difference in loading mode might explain why cohesive failure occurs at lower A in lap-shear tests. Similar parametric study for lap-shear joints is left for further investigations. Suzuki et al. [10] and Sun et al. [11,12] performed DCB tests along interfaces patterned with grooves. However, the present results cannot be applied to the cases investigated by Sun et al. [11,12] as in the absence of grooves, cohesive failure is already reported and the grooves are used to modify the stress state ahead of the crack and not to promote mechanical interlocking. Suzuki et al. [10] performed DCB tests and finite element simulations using cohesive zone elements, considering both cohesive and adhesive failure. This is the only study to which the present results can be compared. They assumed mode-dependent cohesive laws, i.e. different cohesive strength and energy in tension and shear. The groove edges are mainly loaded under shear and therefore the cohesive properties under shear are considered for interfacial failure, while the material filling the grooves is mainly loaded under mode I, hence the tensile cohesive properties are considered. This gives a cohesive strength ratio σ_c^1/σ_c^i equal to 5 and a toughness ratio Γ_c^1/Γ_c^i equal to 4. For a groove depth D about $0.01l_s^1$, and α equal to 0.5, they report a shift from interface to cohesive failure at an aspect ratio, $A = D/L$, about 2.5. As the grooves are much smaller than the adherend thickness, it is assumed that the bending of the adherends can be neglected. Hence, these results are compared to those shown in Fig. 5c in which their transition point is shown. A good match is observed as the SSY model predicts a transition between cohesive and interfacial failure for similar values of σ_c^1/σ_c^i and Γ_c^1/Γ_c^i for these groove dimensions.

4.2. Design criterion based on FE results

Section 3 highlights the influence of the material and interface properties, and the groove dimensions on the failure mechanisms taking place along patterned interfaces. It has been found that the depth D and the length L of the groove have an important influence on the failure mechanisms. A groove aspect ratio D/L equal or larger than 10 induces cohesive failure if $L < l_s^1$. In addition, the stress state at the crack tip also influences the failure mechanism. This stress state depends not only on the loading configuration but also on the relative stiffness of the materials on both sides of the interface. For example, if material 1 is stiffer than material 2, interfacial failure is promoted due to the development of tensile stresses acting along the groove vertices. In the DCB configuration, these tensile stresses additionally arise from the bending of the adherends.

In the present work, the spacing between the grooves has not been discussed because it has been found to not an have influence on the failure mechanisms taking place along the patterned interface for given material and cohesive properties, in agreement with the results of Kim et al. [9]. However, the spacing influences the stress distribution ahead of the crack tip, in the groove walls. The shorter the spacing, the higher the stresses acting on the groove walls, increasing the probability of wall failure, a mechanism not considered in the present case, as shown in Fig. 14. Such failure mechanism has been reported by Maressa et al. [70]. The S/L ratio at which this mechanism will take place depends on the strength of the wall material. Consequently, without considering wall failure, the design criterion of $A \geq 10$ to promote cohesive failure remains valid for any spacing S. Decreased spacing results in a toughening effect due to the shielding effect arising from the presence of a stiffer material ahead of the crack as the grooves wall material 2 is stiffer than material 1 filling the grooves. This is in agreement with the results of Kim et al. [9], who only reported an influence of the spacing on the fracture toughness of the interface.

Two practical design questions arise from these findings when considering cohesive failure as the mechanism to be favored:

- If interface properties are known, any design within the cohesive failure region of the design space is a valid candidate.
- If interface properties are unknown, assume the interface is significantly weaker than the material filling the grooves. In this case, deep grooves with a high aspect ratio (A $\geq$ 10) are recommended. For DCB specimens, a large ratio of groove depth to adherend thickness (D/h_2) is also crucial. This constraint reduces design flexibility compared to the first scenario.

As an example, one considers Γ_c^1/Γ_c^i equal to 1 and σ_c^1/σ_c^i equal to 4. Under these conditions, Fig. 10a predicts interfacial failure even when the groove aspect ratio is 2, if $D = l_s^1$ and $D/h_2 = 0.2$. Conversely, cohesive failure is observed under the same conditions if h_2 is doubled. In the second case, an aspect ratio A of 2 is sufficient to ensure cohesive failure, and therefore long grooves can be machined in the adherend. If the interface properties are unknown, an aspect ratio of about 10 would be recommended to guarantee cohesive failure, which would result in significantly shorter grooves. In more extreme cases, this might even necessitate a change in manufacturing technology. For example, long and deep grooves can be introduced through conventional machining, whereas grooves only of a few tens of micrometers in length or depth would require laser patterning through laser ablation or even more

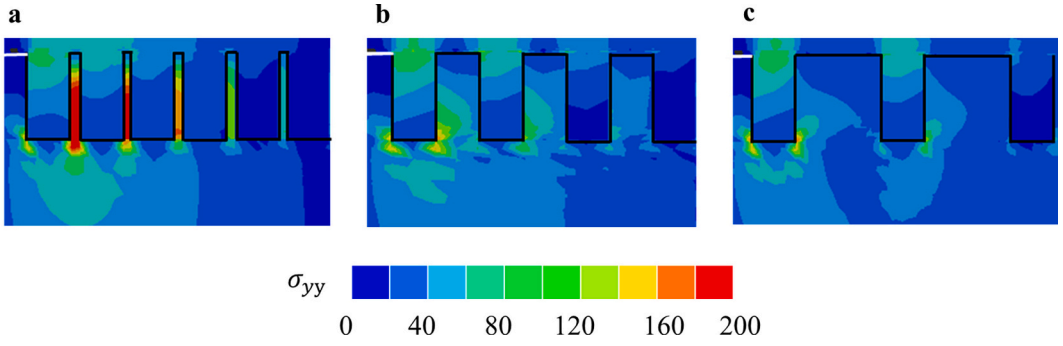

Fig. 14. Normal stress distribution for grooves with $D = l_s^1$, $h_2 = 10l_s^1$, $L = 0.5l_s^1$ and spacing set to a) $S = 0.1l_s^1$, b) $S = 0.5l_s^1$ and c) $S = l_s^1$. σ_c^1/σ_c^i is set to 4 and Γ_c^1/Γ_c^i is set to 2.

advanced (and more expensive) techniques such as lithography. This highlights the trade-off between design goals and manufacturing feasibility. Furthermore, extreme groove geometries can lead to trapped air, altering the failure mechanism, as reported by Andarabi et al. [13], an important practical consideration. This is briefly investigated in Appendix C. The less the groove is filled with material 1, the more interfacial failure is promoted.

Determining interface and material properties, as well as joint dimensions, is crucial for designing the interface pattern and selecting suitable manufacturing technologies. It is important to note that these properties evolve during in-service life, as assemblies may be exposed to chemicals, humidity, and thermal cycles. In humid environments, water ingression reduces material strength, and adsorption at the interface often occurs faster than absorption in the adhesive [71–73]. As a result, interface properties degrade more rapidly, potentially shifting the failure mode from cohesive to interfacial. The degradation rate depends on surface treatment, interface roughness, and pattern [74,75]. A more tortuous interface can slow down water transport, except when voids such as trapped air are present, which facilitate ingression. Under thermal cycling, mismatched thermal expansion coefficients generate tensile residual stresses at the interface, further promoting interfacial failure [76], while temperature variations also affect polymer properties [77]. These examples highlight the need to assess material and interface properties not only after manufacturing but also after exposure to service conditions to ensure proper design.

In general, the advice to design a tough interface is to promote cohesive failure as this leads to higher toughness. This requires having a large groove aspect ratio. However, interface fracture toughness can be influenced by other parameters such as the complete filling of the groove by material 1 [13]. In addition, it is important to note that cohesive failure is assumed to be the toughest mechanism when the groove dimensions range from few micrometers to hundreds of micrometers. Such dimensions are achieved through additive manufacturing or laser ablation. However, Maloney and Fleck [78,79], Cordisco et al. [80] and

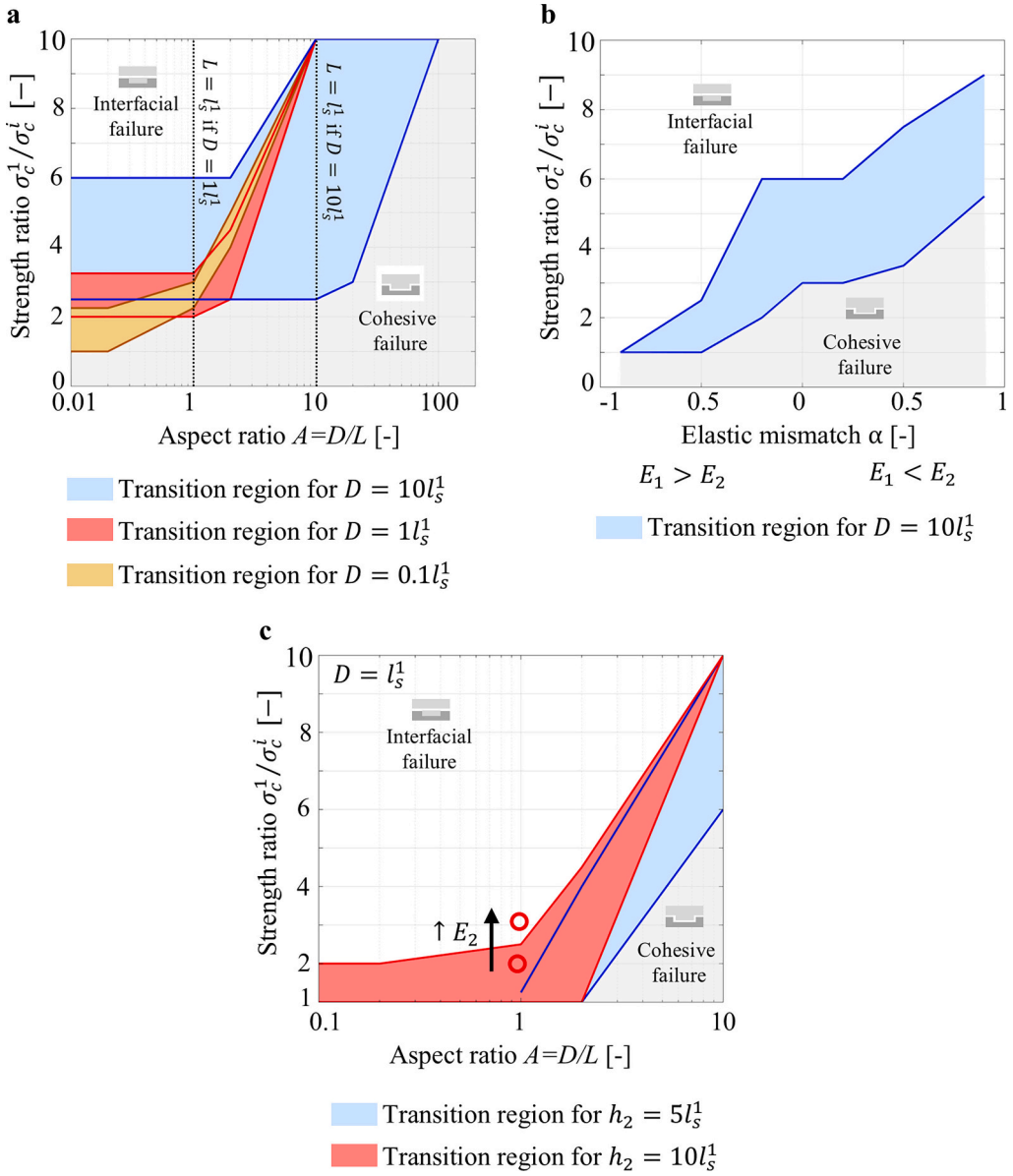

Fig. 15. Summary of the main findings illustrated by failure maps depending on the cohesive strength ratio σ_c^1/σ_c^i. The colored area represent the transition region between the two mechanisms as the critical cohesive strength ratio σ_c^1/σ_c^i depends on the toughness ratio Γ_c^1/Γ_c^i. a) Influence of aspect ratio on the failure mechanism for different groove depths (SSY model). b) Influence of elastic mismatch on the failure mechanism (SSY model) for D $= 10l_s^1$. c) Influence of the groove aspect ratio for $h_2 = 5l_s^1$ and $h_2 = 10l_s^1$ if D I fixed to l_s^1 (DCB model).

Zavattieri et al. [42] dealt with macroscopic patterns with dimensions above 1 mm. In these cases, a crack following the interface pattern results in a strong toughening effect. Hence, adhesive failure can also lead to a toughening effect. Determining the influence of groove dimensions and the failure mechanism on the toughening effect is part of further investigations.

5. Conclusion

Surface patterning with grooves is often investigated as toughening strategy in adhesive joints and other polymer-metal junctions. Depending on the groove dimensions (length L, depth D and spacing S), failure can be either cohesive or interfacial, or a mix of both. Several dimensions have already been investigated previously [9,10,13,22,27]. However, a clear design criterion ensuring cohesive failure has not been established. Crack deflection and penetration are known to be dependent on material and interface strength and toughness [33]. In the present study, the influence of dimensions and cohesive properties is investigated using two cohesive zone models. The different dimensions are compared to the characteristic length scale of the groove material l_s^1. First, a SSY model is implemented to investigate pure mode I disregarding the influence of bending of the adherends taking place in a DCB configuration. For both models, the main conclusions are illustrated in Fig. 15 and are summarized here-below:

- The stronger and the tougher the material filling the grooves, with respect to the interface, the more crack deflection is promoted.
- Deeper grooves (high D) promote mechanical interlocking and, therefore, promote cohesive failure. D/l_s^1 should exceed a value of 10 to avoid interaction with the bottom interface of the groove and avoid interfacial failure.
- Short grooves (low L) promote mechanical interlocking, promoting cohesive failure as shown in Fig. 15a. There is a combined influence with the depth. This led to a minimum aspect ratio D/L equal to 10 to ensure cohesive failure and a groove length shorter than l_s^1.
- The elastic mismatch between the adherend and material filling the grooves influences the transition between the two failure mechanisms. In general, a more compliant material filling the grooves, i.e. material 1, promotes mechanical interlocking, as shown in Fig. 15b. The influence of the elastic mismatch decreases as the groove depth decreases.
- Mode-mixity influences the transition between the two mechanisms. A high Γ_{IIc}/Γ_{Ic} tend to promote cohesive failure while decreasing τ_c/σ_c promotes interfacial failure.

In the DCB configuration, bending of the arms results in tensile stresses acting along the vertical edges of the groove. These stresses promote crack deflection along the interface. To promote cohesive failure:

- Bending strains are minimized by using stiffer or thicker adherends, promoting cohesive failure as shown in Fig. 15c. Although, the adherend thickness has more influence on the failure mechanism than the Young's modulus that is also affecting the elastic mismatch between the adherend and the material filling the grooves (material 1)
- There exists an optimum groove depth as increasing D/h_2 and decreasing D promote interfacial failure.
- An aspect ratio D/L of 10 is found to promote cohesive failure even if the interface is significantly less strong than the material filling the grooves, similar to the SSY model if $L \leq l_s^1$, as shown in Fig. 15c.

To conclude, the failure mechanism taking place along a patterned bimaterial interface depends on the pattern dimensions. The optimal dimensions depend on the material and interface properties, but an aspect ratio A larger or equal to 10 is found to lead to cohesive failure in all investigated cases if $L < l_s^1$. Regarding the DCB configuration, thin adherends and large D/h_2 can shift the critical aspect ratio value towards higher values. However, optimum design also depends on the patterning technique (milling, additive manufacturing, laser ablation). Hence, optimum design is a savant combination of material and interface properties, adherends dimensions and manufacturing technology. The stress-state at the crack tip also influences the results. Minimizing tensile stresses acting along the groove vertices promote cohesive failure.

Owing to the lack of experimental data to compare these numerical results to experiments, experimental studies are recommended as further work.

CRediT authorship contribution statement

Charline van Innis: Writing – original draft, Visualization, Validation, Methodology, Investigation, Formal analysis, Conceptualization. **Julie Teuwen:** Writing – review & editing, Visualization, Validation, Supervision, Methodology, Conceptualization. **Sofia Teixeira de Freitas:** Writing – review & editing, Visualization, Validation, Supervision, Methodology, Funding acquisition, Conceptualization.

Declaration of competing interest

The authors declare that they have no known competing financial interests or personal relationships that could have appeared to influence the work reported in this paper.

Acknowledgments

The authors would like the research consortium “Luchtvaart in Transitie – LiT STC” funding the research project of C. vI. The authors acknowledge Fundação para a Ciência e a Tecnologia (FCT) for its financial support via LAETA (project https://doi.org/10.54499/UID/50022/2025).

Appendix A. Control algorithm for DCB model

In the DCB model, some snap-back instabilities are observed. This happens when interfacial failure, i.e. crack propagation along the groove edges, and when a crack propagating cohesively reaches the upper interface of the groove, which might be characterized by a significantly lower toughness. This results in convergence issues. To avoid them, a control algorithm is implemented, similar to what has been proposed by Martinez-Paneda et al. [48] and Segurado and Lorca [49]. Under displacement controlled conditions, when a snap-back instability takes place, the applied force suddenly drops at the nodes to which the displacement boundary condition is applied. This leads to convergence issues. To avoid this, we need a variable increasing monotonically during the whole loading history. This variable is the relative opening displacement of the crack faces at the location of the first cohesive elements. Relative opening displacement of the crack faces cannot be directly applied as boundary conditions. Hence, it requires to create two auxiliary elements. The first auxiliary element, denoted as El_1, connect the two nodes located at the extremity of the first cohesive element, N_1 and N_2, to a control node, denoted as N_c, as shown in Fig. A1b. The second element, denoted as El_2, connects the two nodes on which the displacement boundary condition are normally applied in a DCB model, N_{top} and N_{bot}, and the control node.

The vertical relative opening displacement of N_1 and N_2 are linearly related to the vertical force applied on the control node, f_{yNc}, (by)

$$f_{yNc} = u_{N1y} - u_{N2y} \tag{A1}$$

The applied vertical loads on N_{top} and N_{bottom} leads to the opening of the DCB and is related to the vertical displacement of the control node, u_{yNc} such that

$$u_{Ncy} = f_{y-Ntop} = -f_{y-Nbot} \tag{A2}$$

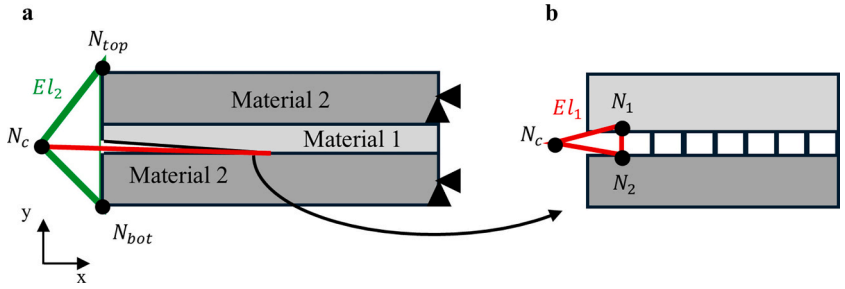

Fig. A1. Definition of the reference and control nodes N_c, and of the auxiliary elements El_1 and El_2 required to implement the control algorithm preventing convergence issues due to snap-back instability.N_1 and N_2 correspond to the top and bottom node of the first cohesive element, respectively, while N_{top} and N_{bot} are the upper left and bottom left node of the DCB geometry, respectively.

This algorithm is implemented into the Abaqus model using user-defined stiffness matrices. More information regarding the implementation can be found in the documentation linked to [48]. In addition, the right end of the DCB is considered as being built-in.

Appendix B. Partly built-in beam

A finite element model is built. It considers a beam of Young's modulus *E*, thickness *h, width B,* and length l. The beam is built-in at its right end, while a displacement is applied at the left side, as shown in Fig. B1. The beam is built-in only over a certain part of its thickness. The length over which it is built-in is denoted as h_e. The beam is model with 4 nodes plane-strain elements with reduced integration (CPE4R). For all simulations, a displacement of 1 mm is applied.

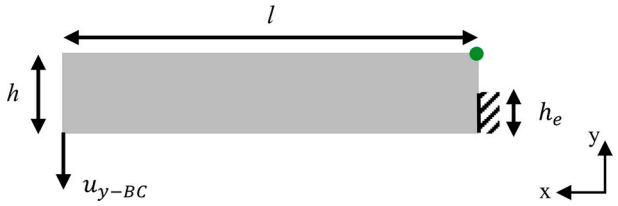

Fig. B1. Schematic of the partly cantilevered beam model. The green dot is the reference node where the horizontal displacement is determined in Fig. C2. h is the total bema thickness, l its length and h_e is the thickness over which the beam is built-in. (For interpretation of the references to colour in this figure legend, the reader is referred to the web version of this article.)

As the beam bends, the part of the right edge, which is built-in, does not move. However, the non-built-in part moves along the *x* and *y* direction. The horizontal displacement of the right top node is determined for several h_e/h ratios and given displacement u_{y-BC}. Fig. B2 shows that as h_e/h increases, the vertical displacement of the top right node decreases.

A parallel has to be made with the patterned DCB arm. The non-built-in part corresponds to the groove vertical edge. Consequently, the deeper the groove (lower h_e/h), the higher the horizontal strains acting along the interface as the vertical displacements are larger.

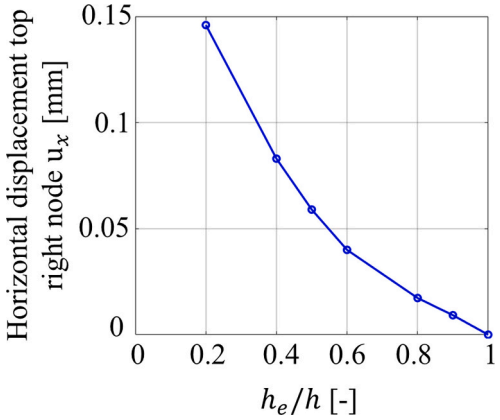

Fig. B2. Evolution of the horizontal displacement at the top right node (green dot in Fig. B1) of the partly built-in beam with h_e/h. (For interpretation of the references to colour in this figure legend, the reader is referred to the web version of this article.)

Appendix C. Partial filling of grooves

Imperfect filling of the grooves is expected to shift the transition curve towards lower cohesive strength ratio, promoting interfacial failure. Two main reasons can be attributed to this effect. First, imperfect filling results in stress in higher stress concentrations. Secondly, the bonded area is lower as the filling material (material 1) is not bonded to the adherend material (material 2). In order to address this comment, simulations have been run for $L = D = l_s^1$ and $L = D = 10l_s^1$, with $\alpha = 0$ by modifying the python code generating the mesh to remove 10 and 50% of the elements at the bottom of the groove. Simulations are only run for the SSY model.

Fig. C1a shows that imperfect filling results in a leftward shift of the transition curve, promoting interfacial failure. The less the groove is filled, the more interfacial failure is promoted. Figs. C1b to e show the stress distributions near the groove for $D = L = l_s^1$, $\sigma_c^1/\sigma_c^i = 2.5$ and $\Gamma_c^1/\Gamma_c^i = 2$. It is observed that incomplete filling decreases the tensile stresses. Hence, mainly shear stresses act around the crack tip, resulting in interfacial failure. In addition, stress concentrations are found at the bottom corner of the filling material, initiating interfacial failure at the top and bottom corner of filling material edge.

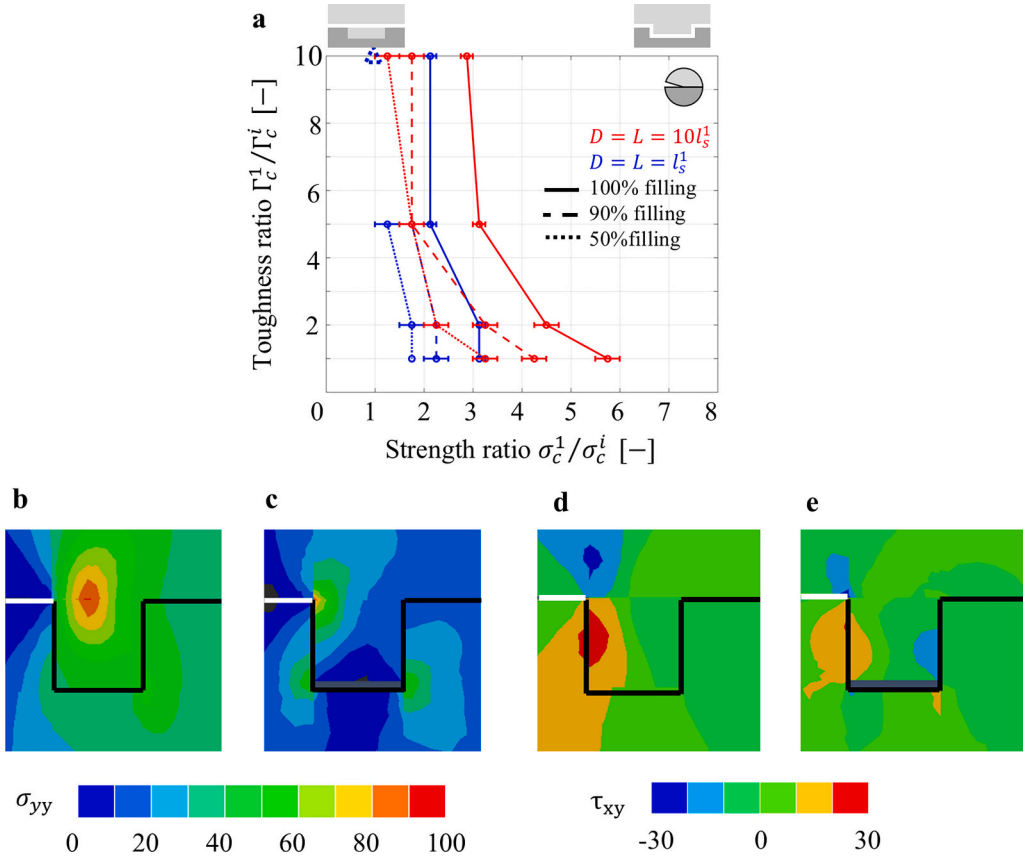

Fig. C1. a) Influence of the groove depth D and groove filling on the transition between cohesive (left of the curve) and interfacial failure (right of the curve) depending on Γ_c^1/Γ_c^i and σ_c^1/σ_c^i. b-c) Tensile stress distribution for b) complete filling and c) 90% filling. d-e) Shear stress distribution for d) complete filling and e) 90% filling. b-e) The snapshots are taken for a remote K^∞ equal to 1.58 MPa$\sqrt{m}$.

Appendix A. Supplementary data

Supplementary data to this article can be found online at https://doi.org/10.1016/j.tafmec.2026.105586.

Data availability

Data will be made available on request.

References

[1] M. Barile, L. Lecce, M. Lannone, S. Pappadà, P. Roberti, Thermoplastic composites for aerospace applications, in: S. Pantelakis, K. Tserpes (Eds.), Revolutionizing Aircraft Materials and Processes, Springer International Publishing, 2020, https://doi.org/10.1007/978-3-030-35346-9.

[2] A.V. Pocius, Adhesion and adhesives technology, third edit, Carl Hanser Verlag GmbH & co, KG (2012), https://doi.org/10.3139/9783446431775.fm.

[3] C. Ageorges, L. Ye, M. Hou, Advances in fusion bonding techniques for joining thermoplastic matrix composites: a review, Compos. Part A Appl. Sci. Manuf. 32 (2001) 839–857, https://doi.org/10.1016/S1359-835X(00)00166-4.

[4] T.J. Ahmed, D. Stavrov, H.E.N. Bersee, A. Beukers, Induction welding of thermoplastic composites-an overview, Compos. Part A Appl. Sci. Manuf. 37 (2006) 1638–1651, https://doi.org/10.1016/j.compositesa.2005.10.009.

[5] C. Ageorges, L. Ye, Resistance welding of metal/thermoplastic composite joints, J. Thermoplast. Compos. Mater. 14 (2001) 449–475, https://doi.org/10.1106/PN74-QXKH-7XBE-XKF5.

[6] V.M. Marinosci, W.J.B. Grouve, M.B. de Rooij, S. Wijskamp, R. Akkerman, Effect of grit-blasting on the fracture toughness of hybrid titanium-thermoplastic composite joints, Int. J. Adhes. Adhes. 109 (2021) 102893, https://doi.org/10.1016/j.ijadhadh.2021.102893.

[7] Y. Boutar, S. Naïmi, S. Mezlini, L.F.M. Da Silva, M. Hamdaoui, M. Ben Sik Ali, Effect of adhesive thickness and surface roughness on the shear strength of aluminium one-component polyurethane adhesive single-lap joints for automotive applications, J. Adhes. Sci. Technol. 30 (2016) 1913–1929, https://doi.org/10.1080/01694243.2016.1170588.

[8] M. Shahid, S.A. Hashim, Effect of surface roughness on the strength of cleavage joints, Int. J. Adhes. Adhes. 22 (2002) 235–244, https://doi.org/10.1016/S0143-7496(01)00059-8.
[9] W.S. Kim, I.H. Yun, J.J. Lee, H.T. Jung, Evaluation of mechanical interlock effect on adhesion strength of polymer-metal interfaces using micro-patterned surface topography, Int. J. Adhes. Adhes. 30 (2010) 408–417, https://doi.org/10.1016/j.ijadhadh.2010.05.004.
[10] T. Suzuki, R. Matsuzaki, A. Todoroki, Y. Mizutani, Crack growth analysis of a composite/adhesive interface toughened by in-mold surface preparation, Int. J. Adhes. Adhes. 42 (2013) 36–43, https://doi.org/10.1016/j.ijadhadh.2013.01.008.
[11] F. Sun, C.I. Pruncu, P. Penchev, J. Jiang, S. Dimov, B.R.K. Blackman, Influence of surface micropatterns on the mode I fracture toughness of adhesively bonded joints, Int. J. Adhes. Adhes. 103 (2020) 102718, https://doi.org/10.1016/j.ijadhadh.2020.102718.
[12] F. Sun, P. Penchev, C.I. Pruncu, J. Wang, C. Pargeter, Y. Wang, C. Li, S. Dimov, J. Jiang, B.R.K. Blackman, On enhancement of fracture resistance of adhesive joints by surface micropatterning using a femtosecond laser, J. Mater. Process. Technol. 315 (2023), https://doi.org/10.1016/j.jmatprotec.2023.117904.
[13] A.A. Andarabi, K. Shelesh-Nezhad, T.N. Chakherlou, The effect of laser surface structuring patterns on the interfacial resistance of aluminum joints bonded with epoxy adhesive, Int. J. Adhes. Adhes. 114 (2022) 103101, https://doi.org/10.1016/j.ijadhadh.2022.103101.
[14] A.T.T. Nguyen, M. Brandt, A.C. Orifici, S. Feih, Hierarchical surface features for improved bonding and fracture toughness of metal-metal and metal-composite bonded joints, Int. J. Adhes. Adhes. 66 (2016) 81–92, https://doi.org/10.1016/j.ijadhadh.2015.12.005.
[15] X. Liu, H. Zhu, Y. Xie, L. Xu, N. Lin, L. Lu, Optimization of microstructural morphology via laser processing to enhance the bond strength of Al-CFRP, J. Reinf. Plast. Compos. 40 (2021) 463–473, https://doi.org/10.1177/07316844209730666.
[16] H. Wan, J. Min, B.E. Carlson, J. Lin, C. Sun, Spindle-shaped surface microstructure inspired by directional water collection biosystems to enhance interfacial wetting and bonding strength, ACS Appl. Mater. Interfaces 13 (2021) 13760–13770, https://doi.org/10.1021/acsami.0c21857.
[17] T. Bagnato, A.R. Ravindran, A. Mirabedini, R.B. Ladani, E. Kandare, A.C. Orifici, P. Chang, J. Wang, A.P. Mouritz, Superior interfacial toughening of hybrid metal-composite structural joints using 3D printed pins, Compos. Part A Appl. Sci. Manuf. 168 (2023) 107479, https://doi.org/10.1016/j.compositesa.2023.107479.
[18] N. Naat, Y. Boutar, S. Naïmi, S. Mezlini, L.F.M. Da Silva, Effect of surface texture on the mechanical performance of bonded joints: a review, J. Adhes. Dent. 99 (2023) 166–258, https://doi.org/10.1080/00218464.2021.2008370.
[19] Z. Kang, Z. Shi, Y. Lei, Q. Xie, J. Zhang, Effect of the surface morphology on the bonding performance of metal/composite hybrid structures, Int. J. Adhes. Adhes. 111 (2021), https://doi.org/10.1016/j.ijadhadh.2021.102944.
[20] T. Alderucci, C. Borsellino, G. Di Bella, Effect of surface pattern on strength of structural lightweight bonded joints for marine applications, Int. J. Adhes. Adhes. 117 (2022), https://doi.org/10.1016/j.ijadhadh.2021.103005.
[21] L.F.M. Da Silva, N.M.A.J. Ferreira, V. Richter-Trummer, E.A.S. Marques, Effect of grooves on the strength of adhesively bonded joints, Int. J. Adhes. Adhes. 30 (2010) 735–743, https://doi.org/10.1016/j.ijadhadh.2010.07.005.
[22] E. Akman, M.Ö. Bora, O. Çoban, B.G. Oztoprak, Laser-induced groove optimization for Al/CFRP adhesive joint strength, Int. J. Adhes. Adhes. 107 (2021), https://doi.org/10.1016/j.ijadhadh.2021.102830.
[23] Z. Wang, X. Bi, B. Liu, M. Xu, Z. Dong, Adhesion enhancement of PEEK/6161-T6 FLJ joints via laser surface modification, Compos. Part B Eng. 216 (2021), https://doi.org/10.1016/j.compositesb.2021.108797.
[24] S. Verma, C.K. Yang, C.H. Lin, J.Y. Jeng, Additive manufacturing of lattice structures for high strength mechanical interlocking of metal and resin during injection molding, Addit. Manuf. 49 (2022), https://doi.org/10.1016/j.addma.2021.102463.
[25] J. Moritz, P. Götze, T. Schiefer, L. Stepien, A. Klotzbach, J. Standfuß, E. López, F. Brückner, C. Leyens, Additive manufacturing of titanium with different surface structures for adhesive bonding and thermal direct joining with fiber-reinforced polyether-ether-ketone (PEEK) for lightweight design applications, Metals (Basel). 11 (2021) 1–14, https://doi.org/10.3390/met11020265.
[26] T. Suzuki, R. Matsuzaki, A. Todoroki, Y. Mizutani, Prediction of the macroscopic fracture toughness of a composite/adhesive interface with periodic surface microstructures, Int. J. Adhes. Adhes. 60 (2015) 16–22, https://doi.org/10.1016/j.ijadhadh.2015.03.003.
[27] Y. Yukimoto, R. Matsuzaki, A. Todoroki, Mode II interfacial fracture toughness of composite/adhesive interfaces obtained by in-mold surface modification, Int. J. Adhes. Adhes. 50 (2014) 191–198, https://doi.org/10.1016/j.ijadhadh.2014.01.034.
[28] F. Wang, H. Bu, J. Luo, P. Zhang, L. Wang, X. Zhan, Influence of different micro-pattern types on interface characteristic and mechanical property of CFRTP/aluminum alloy laser bonding joint, Int. J. Adv. Manuf. Technol. 120 (2022) 3543–3557, https://doi.org/10.1007/s00170-022-08748-6.
[29] N. Naat, Y. Boutar, S. Naïmi, S. Mezlini, L.F.M. da Silva, A.H. Bashiri, Influence of bio-inspired surface texture of additively manufactured 17-4 PH stainless steel adherends on the strength of adhesively bonded joints, Int. J. Adhes. Adhes. 126 (2023), https://doi.org/10.1016/j.ijadhadh.2023.103478.
[30] L.A. Ardila-Rodríguez, C. Rans, J.A. Poulis, Effect of surface morphology on the Ti–Ti adhesive bond performance of Ti6Al4V parts fabricated by selective laser melting, Int. J. Adhes. Adhes. 110 (2021), https://doi.org/10.1016/j.ijadhadh.2021.102918.
[31] Z. Fielden-Stewart, T. Coope, D. Bacheva, B.C. Kim, Effect of the surface morphology of SLM printed aluminium on the interfacial fracture toughness of metal-composite hybrid joints, Int. J. Adhes. Adhes. 105 (2021), https://doi.org/10.1016/j.ijadhadh.2020.102779.
[32] E. Paz, J.J. Narbón, J. Abenojar, M. Cledera, J.C. del Real, Influence of acrylic adhesive viscosity and surface roughness on the properties of adhesive joint, J. Adhes. 92 (2016) 877–891, https://doi.org/10.1080/00218464.2015.1051221.
[33] J. Parmigiani, M. Thouless, The roles of toughness and cohesive strength on crack deflection at interfaces, J. Mech. Phys. Solids 54 (2006) 266–287, https://doi.org/10.1016/j.jmps.2005.09.002.
[34] M.-Y. He, J.W. Hutchinson, Crack deflection at an interface between dissimilar elastic materials, Int. J. Solids Struct. 25 (1989) 1053–1067, https://doi.org/10.1016/0020-7683(89)90021-8.
[35] E. Martin, D. Leguillon, C. Lacroix, A revisited criterion for crack deflection at an interface in a brittle bimaterial, Compos. Sci. Technol. 61 (2001) 1671–1679, https://doi.org/10.1016/S0266-3538(01)00067-7.
[36] D. Leguillon, C. Lacroix, E. Martin, Interface debonding ahead of a primary crack, J. Mech. Phys. Solids 48 (2000) 2137–2161, https://doi.org/10.1016/S0022-5096(99)00101-5.
[37] ISO, ISO25217 Adhesives — Determination of the mode 1 adhesive fracture energy of structural adhesive joints using double cantilever beam and tapered double cantilever beam specimens, 2014.
[38] R.A.A. Lima, R. Tao, A. Bernasconi, M. Carboni, N. Carrere, S. Teixeira de Freitas, Uncovering the toughening mechanisms of bonded joints through tailored CFRP layup, Compos. Part B Eng. 263 (2023), https://doi.org/10.1016/j.compositesb.2023.110853.
[39] W. Wang, R. Lopes Fernandes, S. Teixeira De Freitas, D. Zarouchas, R. Benedictus, How pure mode I can be obtained in bi-material bonded DCB joints: a longitudinal strain-based criterion, Compos. Part B Eng. 153 (2018) 137–148, https://doi.org/10.1016/j.compositesb.2018.07.033.
[40] J.W. Hutchinson, V. Tvergaard, The relation between crack growth resistance and fracture process parameters elastic-plastic solids, J. Mech. Phys. Solids 40 (1992) 1377–1397.
[41] V. Tvergaard, J.W. Hutchinson, The influence of plasticity on mixed mode interface toughness, J. Mech. Phys. Solids 41 (1993) 1119–1135, https://doi.org/10.1016/0022-5096(93)90057-M.
[42] P.D. Zavattieri, L.G. Hector, A.F. Bower, Determination of the effective mode-I toughness of a sinusoidal interface between two elastic solids, Int. J. Fract. 145 (2007) 167–180, https://doi.org/10.1007/s10704-007-9109-y.
[43] C. van Innis, T. Pardoen, Thickness-dependent selection of adhesive joints, J. Adhes. Dent. 100 (2023) 1155–1208, https://doi.org/10.1080/00218464.2023.2294131.
[44] J. Dundurs, Discussion: edge-bonded dissimilar orthogonal elastic wedges under Normal and shear loading, J. Appl. Mech. 3 (1969) 650–652, https://doi.org/10.1115/1.3564739.
[45] S. Dépinoy, T.J. Massart, S. Godet, T. Pardoen, On the mode I toughness of adhesive bonds exhibiting strain-softening and re-hardening, Int. J. Solids Struct. 162 (2019) 1–13, https://doi.org/10.1016/j.ijsolstr.2018.11.026.
[46] S. Dépinoy, F. Strepenne, T.J. Massart, S. Godet, T. Pardoen, Interface toughening in multilayered systems through compliant dissipative interlayers, J. Mech. Phys. Solids 130 (2019) 1–20, https://doi.org/10.1016/j.jmps.2019.05.013.
[47] T. Pardoen, T. Ferracin, C.M. Landis, F. Delannay, Constraint effects in adhesive joint fracture, J. Mech. Phys. Solids 53 (2005) 1951–1983, https://doi.org/10.1016/j.jmps.2005.04.009.
[48] E. Martínez-Pañeda, S. del Busto, C. Betegón, Non-local plasticity effects on notch fracture mechanics, Theor. Appl. Fract. Mech. 92 (2017) 276–287, https://doi.org/10.1016/j.tafmec.2017.09.007.
[49] J. Segurado, J. LLorca, A new three-dimensional interface finite element to simulate fracture in composites, Int. J. Solids Struct. 41 (2004) 2977–2993, https://doi.org/10.1016/j.ijsolstr.2004.01.007.
[50] A. Turon, C.G. Davila, P.P. Camanho, J. Costa, An engineering solution for mesh size effects in the simulation of delamination using cohesive zone models, Eng. Fract. Mech. 74 (2007) 1665–1682, https://doi.org/10.1016/j.engfracmech.2006.08.025.
[51] S.A. Ponnusami, J. Krishnasamy, S. Turteltaub, S. van der Zwaag, Elucidating the effect of cohesive zone length in fracture simulations of particulate composites, Eng. Fract. Mech. 268 (2022), https://doi.org/10.1016/j.engfracmech.2022.108431.
[52] A. Hillerborg, M. Modéer, P.-E. Petersson, Analysis of crack formation and crack growth in concrete by means of fracture mechanics and finite elements, Cem. Concr. Res. 6 (1976) 773–781, https://doi.org/10.1016/0008-8846(76)90007-7.
[53] J.R. Rice, The mechanics of earthquake rupture, in: B.E. Dziewonski, AM (Eds.), Proceedings of the International School of Physics Enrico Fermi, 1980, pp. 555–649.
[54] K. Ha, H. Baek, K. Park, Convergence of fracture process zone size in cohesive zone modeling, Appl. Math. Model. 39 (2015) 5828–5836, https://doi.org/10.1016/j.apm.2015.03.030.
[55] J. Xie, A.M. Waas, M. Rassaian, Estimating the process zone length of fracture tests used in characterizing composites, Int. J. Solids Struct. 100–101 (2016) 111–126, https://doi.org/10.1016/j.ijsolstr.2016.07.018.
[56] M.T. Tilbrook, I.E. Reimanis, K. Rozenburg, M. Hoffman, Effects of plastic yielding on crack propagation near ductile/brittle interfaces, Acta Mater. 53 (2005) 3935–3949, https://doi.org/10.1016/j.actamat.2005.04.045.
[57] N.A. Fleck, J.W. Hutchinson, Z. Suo, Crack path selection in a brittle adhesive layer, Int. J. Solids Struct. 27 (1991) 1683–1703, https://doi.org/10.1016/0020-7683(91)90069-R.
[58] J.G. Kirchhoff, N.T. Heathman, T. Yap, P. Koirala, T.B. Hudson, M. Tehrani, Interlaminar bonding in thermoplastic composites: a comparative analysis of laser

AFP and post-processing, Compos. Part B Eng. 294 (2025), https://doi.org/10.1016/j.compositesb.2025.112156.
[59] M.F. Talbott, G.S. Springer, L.A. Berglund, The effects of crystallinity on the mechanical properties of PEEK polymer and graphite Fiber reinforced PEEK, J. Compos. Mater. 21 (1987) 1056–1081, https://doi.org/10.1177/002199838702101104.
[60] V.M. Marinosci, N.G.J. Helthuis, L. Chu, W.J.B. Grouve, M.B. de Rooij, S. Wijskamp, R. Akkerman, The role of process induced polymer morphology on the fracture toughness of titanium–PEKK interfaces, Eng. Fract. Mech. 268 (2022), https://doi.org/10.1016/j.engfracmech.2022.108475.
[61] A. Sharma, A. Shivaie Kojouri, J. Fan, A.P. Vassilopoulos, V. Michaud, K. A. Kalteremidou, D. Van Hemelrijck, W. Van Paepegem, Combined computational-experimental investigation of residual stresses and pre-cracking in mode I behaviour of thick adhesively bonded GFRP composite joints, Compos. Struct. 351 (2025), https://doi.org/10.1016/j.compstruct.2024.118549.
[62] J.W. Hutchinson, Z. Suo, Mixed mode cracking in layered materials, Adv. Appl. Mech. 29 (1992) 262.
[63] Z. Suo, J.W. Hutchinson, Interface crack between two elastic layers, Int. J. Fract. 43 (1990) 1–18, https://doi.org/10.1007/BF00018123.
[64] M.-Y. He, J.W. Hutchinson, Kinking of a crack out of an Interface, J. Appl. Mech. 56 (1989) 270–278, https://doi.org/10.1115/1.3176078.
[65] J.W. Hutchinson, M.E. Mear, J.R. Rice, Crack paralleling an Interface between dissimilar materials, J. Appl. Mech. 109 (1987).
[66] N.J. Al-Ramahi, R. Joffe, J. Varna, Criteria for crack path deviation in adhesive layer of bi-material DCB specimen, Compos. Part A Appl. Sci. Manuf. 147 (2021) 106408, https://doi.org/10.1016/j.compositesa.2021.106408.
[67] B. Blackman, F. Sun, S. Teixeira de Freitas, S. de Barros, M. Moreira Arouche, A. Ivankovic, 17 - understanding fracture mode-mixity and its effects on bond performance, in: D.A. Dillard (Ed.), Advances in Structural Adhesive Bonding, 2, Woodhead Publishing, 2023, pp. 579–613, https://doi.org/10.1016/B978-0-323-91214-3.00015-6.
[68] H.K. Thakur, G. Prasad, Mode 1, mode II, and mixed mode I/II fracture behavior of laminated structures, in: A. Kumar, Y. Kumar Singla, M.R. Maughan (Eds.), Fracture Behavior of Nanocomposites and Reinforced Laminate Structures, Springer Nature, Switzerland, Cham, 2024, pp. 123–155, https://doi.org/10.1007/978-3-031-68694-8_6.
[69] H. Sharma, A. Singh, Combined phase-field and cohesive zone modeling for mixed-mode fracture in polymer composites, Eng. Comput. 41 (2025) 3005–3033, https://doi.org/10.1007/s00366-025-02134-y.
[70] P. Maressa, L. Anodio, A. Bernasconi, A.G. Demir, B. Previtali, Effect of surface texture on the adhesion performance of laser treated Ti6Al4V alloy, J. Adhes. Dent. 91 (2014) 518–537, https://doi.org/10.1080/00218464.2014.933809.
[71] K. Wapner, G. Grundmeier, Spatially resolved measurements of the diffusion of water in a model adhesive/silicon lap joint using FTIR-transmission-microscopy, Int. J. Adhes. Adhes. 24 (2004) 193–200, https://doi.org/10.1016/j.ijadhadh.2003.09.008.
[72] M.P. Zanni-Deffarges, M.E.R. Shanahan, Diffusion of water into an epoxy adhesive: comparison between bulk behaviour and adhesive joints, Int. J. Adhes. Adhes. 15 (1995) 137–142.
[73] A. Mubashar, I.A. Ashcroft, G.W. Critchlow, A.D. Crocombe, Moisture absorption-desorption effects in adhesive joints, Int. J. Adhes. Adhes. 29 (2009) 751–760, https://doi.org/10.1016/j.ijadhadh.2009.05.001.
[74] J.P.B. van Dam, S.T. Abrahami, A. Yilmaz, Y. Gonzalez-Garcia, H. Terryn, J.M. C. Mol, Effect of surface roughness and chemistry on the adhesion and durability of a steel-epoxy adhesive interface, Int. J. Adhes. Adhes. 96 (2020) 102450, https://doi.org/10.1016/j.ijadhadh.2019.102450.
[75] S.G. Croll, Surface roughness profile and its effect on coating adhesion and corrosion protection: a review, Prog. Org. Coat. 148 (2020), https://doi.org/10.1016/j.porgcoat.2020.105847.
[76] G.R. Humfeld, D.A. Dillard, Residual stress development in adhesive joints subjected to thermal cycling, J. Adhes. Dent. 65 (1998) 277–306, https://doi.org/10.1080/00218469808012250.
[77] N. Klavzer, J. Chevalier, C. Breite, X.P. Morelle, Y. Swolfs, T. Pardoen, Master trends in the elasto-viscoplastic behaviour of highly cross-linked epoxy resins, Mech. Time. Depend. Mater. 29 (2025), https://doi.org/10.1007/s11043-025-09804-w.
[78] K. Maloney, N. Fleck, Damage tolerance of an architected adhesive joint, Int. J. Solids Struct. 132–133 (2018) 9–19, https://doi.org/10.1016/j.ijsolstr.2017.06.010.
[79] K. Maloney, N. Fleck, Tear resistance of a square-wave joint: experiment versus cohesive zone model, Int. J. Adhes. Adhes. 84 (2018) 9–17, https://doi.org/10.1016/j.ijadhadh.2018.02.008.
[80] F.A. Cordisco, P.D. Zavattieri, L.G. Hector, B.E. Carlson, Mode I fracture along adhesively bonded sinusoidal interfaces, Int. J. Solids Struct. 83 (2016) 45–64, https://doi.org/10.1016/j.ijsolstr.2015.12.028.